

# JGR Atmospheres

## RESEARCH ARTICLE









10.1029/2024JD041297

# CO<sub>2</sub> Emissions Estimate From Mexico City Using Ground- and Space-Based Remote Sensing



### Special Collection:

Observing CO<sub>2</sub> from space: A Decade of progress from NASAs Orbiting Carbon Observatories (OCO-2 and OCO-3)

Ke Che<sup>1,2</sup> , Thomas Lauvaux<sup>2</sup>, Noemie Taquet<sup>3</sup>, Wolfgang Stremme<sup>3</sup>, Yang Xu<sup>1</sup> , Carlos Alberti<sup>4</sup> , Morgan Lopez<sup>1</sup> , Agustín García-Reynoso<sup>3</sup> , Philippe Ciais<sup>1</sup> , Yi Liu<sup>5</sup>, Michel Ramonet<sup>1</sup> , and Michel Grutter<sup>3</sup> 

<sup>1</sup>Laboratoire des Sciences du Climat et de l'Environnement, IPSL, CEA-CNRS-UVSQ, Université Paris-Saclay, Gif sur Yvette Cedex, France, <sup>2</sup>Groupe de Spectrométrie Moléculaire et Atmosphérique, University of Reims Champagne Ardenne, Reims, France, <sup>3</sup>Centro de Ciencias de la Atmósfera, Universidad Nacional Autónoma de México, Mexico City, Mexico, <sup>4</sup>Karlsruhe Institute of Technology, Institute of Meteorology and Climate Research, Karlsruhe, Germany, <sup>5</sup>Institute of Atmospheric Physics, Chinese Academy of Sciences, Beijing, China

### Key Points:

- A high-resolution computational inversion system is developed with Fourier transform infrared (FTIR) and OCO-3 Snapshot Area Map (SAM) observations to improve the urban CO<sub>2</sub> emissions
- FTIR analysis revealed overestimations in current fossil fuel (FF) and biogenic CO<sub>2</sub> emissions over Mexico City
- Inversion constrained by temporally matched observations from OCO-3 and FTIR revealed consistent corrections for FF priors

### Supporting Information:

Supporting Information may be found in the online version of this article.

### Correspondence to:

K. Che,  
[ke.che@lscce.ipsl.fr](mailto:ke.che@lscce.ipsl.fr)

### Citation:

Che, K., Lauvaux, T., Taquet, N., Stremme, W., Xu, Y., Alberti, C., et al. (2024). CO<sub>2</sub> emissions estimate from Mexico City using ground- and space-based remote sensing. *Journal of Geophysical Research: Atmospheres*, 129, e2024JD041297. <https://doi.org/10.1029/2024JD041297>

Received 9 APR 2024

Accepted 30 SEP 2024

### Author Contributions:

**Conceptualization:** Ke Che  
**Data curation:** Noemie Taquet, Wolfgang Stremme, Carlos Alberti, Morgan Lopez, Agustín García-Reynoso, Michel Ramonet, Michel Grutter

**Abstract** The Mexico City Metropolitan Area (MCMA) stands as one of the most densely populated urban regions globally. To quantify the urban CO<sub>2</sub> emissions in the MCMA, we independently assimilated observations from a dense column-integrated Fourier transform infrared (FTIR) network and OCO-3 Snapshot Area Map observations between October 2020 and May 2021. Applying a computationally efficient analytical Bayesian inversion technique, we inverted for surface fluxes at high spatio-temporal resolutions (1-km and 1-hr). The fossil fuel (FF) emission estimates of 5.08 and 6.77 GgCO<sub>2</sub>/hr reported by the global and local emission inventories were optimized to 4.85 and 5.51 GgCO<sub>2</sub>/hr based on FTIR observations over this 7 month period, highlighting a convergence of posterior estimates. The modeled biogenic flux estimate of −0.14 GgCO<sub>2</sub>/hr was improved to −0.33 to −0.27 GgCO<sub>2</sub>/hr, respectively. It is worth noting that utilizing observations from three primary sites significantly enhanced the accuracy of estimates (13.6 ~29.2%) around the other four. Using FTIR posterior estimates can improve simulation with the OCO-3 data set. OCO-3 shows a similar decreasing trend in FF emissions (from 6.37 GgCO<sub>2</sub>/hr to 6.36 and 5.04 GgCO<sub>2</sub>/hr) as FTIR, but its correction trends for biogenic sources differ, changing from 0.37 to 0.48 GgCO<sub>2</sub>/hr. The primary reason is OCO-3's lower temporal sampling density. Aligning the FTIR inversion timing with that of OCO-3 yielded comparable corrections for FF emissions, yet discrepancies in biogenic emissions persisted, which can be attributed to their different sampling locations in the rural region and discrepancy in XCO<sub>2</sub> observations. Our findings mark a significant step toward validating OCO-3 and FTIR inversion results in metropolitan region.

**Plain Language Summary** Urban areas are significant hotspots for CO<sub>2</sub> emissions due to their high energy consumption, prompting a strong push toward ambitious greenhouse gas reduction initiatives. Our study harnessed data from the OCO-3 satellite and an extensive ground-based sensor network to map CO<sub>2</sub> concentrations on an intra-city scale, aiming to update outdated emission inventories. We delved into the effects of observed CO<sub>2</sub> gradient differences on the optimization results, leveraging these two distinct data sources. Although both OCO-3 satellite and ground-based observations offer detailed insights into Mexico City's urban region, they reveal discrepancies in the sampling of rural area data. The local FF inventory, when constrained by ground-based observations, indicates an 18.73% overestimation, whereas the OCO-3 data set points to only a 6.44% overestimation. Our findings highlight that utilizing ground-based observations exclusively during OCO-3 overpass times aligns the correction from ground-based data (6.41% overestimation) with that derived from the OCO-3 data. However, biogenic emissions optimization differs significantly, primarily due to OCO-3's limited rural observations, the rural sampling locations, and the discrepancies in observed XCO<sub>2</sub> values in these data sets.

## 1. Introduction

Cities and city agglomerations, serving as hubs for approximately 57% of the global population (Dorrell et al., 2024), are accountable for over 80% of energy consumption and have produced approximately 75% of the global carbon dioxide (CO<sub>2</sub>) emissions in the past decades, thus pose a serious threat to global CO<sub>2</sub> emissions control (Hong et al., 2022). Numerous cities have committed to reducing CO<sub>2</sub> emissions to mitigate the accelerating impact of climate change resulting from human activities (Ahn et al., 2023). The monitoring and

© 2024. The Author(s).

This is an open access article under the terms of the [Creative Commons Attribution-NonCommercial-NoDerivs License](https://creativecommons.org/licenses/by/4.0/), which permits use and distribution in any medium, provided the original work is properly cited, the use is non-commercial and no modifications or adaptations are made.

**Formal analysis:** Ke Che, Thomas Lauvaux, Yang Xu  
**Funding acquisition:** Michel Ramonet, Michel Grutter  
**Investigation:** Ke Che  
**Methodology:** Ke Che, Thomas Lauvaux  
**Resources:** Noemie Taquet, Wolfgang Stremme, Carlos Alberti, Morgan Lopez, Agustín García-Reynoso, Michel Ramonet, Michel Grutter  
**Software:** Ke Che, Agustín García-Reynoso  
**Supervision:** Thomas Lauvaux  
**Validation:** Ke Che, Yang Xu  
**Visualization:** Ke Che  
**Writing – original draft:** Ke Che  
**Writing – review & editing:** Thomas Lauvaux, Noemie Taquet, Wolfgang Stremme, Carlos Alberti, Agustín García-Reynoso, Philippe Ciais, Michel Ramonet, Michel Grutter

quantification of CO<sub>2</sub> emissions in cities offer valuable insights for policymakers to draft and implement effective carbon reduction strategies (Gately & Hutyra, 2017; Gately et al., 2015; Gurney et al., 2015; Lauvaux et al., 2020).

Two prevalent methodologies for quantifying CO<sub>2</sub> emissions in urban regions are the “bottom-up” and “top-down” approaches. The first involves the disaggregation of national or provincial statistical data over urban areas or the aggregation of various contributors, utilizing various “proxy” activity data sets, such as the emission factors from industry, traffic and road maps, nightlight information, fuel consumption, etc (Guo et al., 2023). This method encounters challenges not only in obtaining the latest data but also introduces significant uncertainties arising from the diversity in methods and tools (G. Chen et al., 2019; Gately & Hutyra, 2017; Oda et al., 2019). Despite concerted efforts in bottom-up urban inventories to address issues such as substantial latency and resolution problems through innovations such as near-real-time carbon monitoring inventories for cities (Huo et al., 2022), there persists a lack of validation to support city-wide urban CO<sub>2</sub> planning. In contrast, “top-down” atmospheric observations offer a more comprehensive perspective, furnishing robust validation or updates for bottom-up inventories but often lacking the granularity to evaluate specific mitigation actions at the sectoral or district levels (Gurney et al., 2019; Lauvaux et al., 2016; Newman et al., 2016).

Observed urban CO<sub>2</sub> enhancements can provide valuable information in quantifying urban CO<sub>2</sub> emissions. Specifically, total column measurements offer distinct advantages over in situ measurements since these exhibit reduced sensitivity to vertical transport errors (Lauvaux & Davis, 2014). Thus, the three-dimensional perspective in in situ measurements are simplified into a more relevant two-dimensional (2-D) view, closely aligned with the horizontally distributed emissions (Wunch et al., 2011). This characteristic proves advantageous for background selection. Since CO<sub>2</sub> is an inert gas, most of the observed CO<sub>2</sub> concentration comes from long-range and medium-range air masses (so called “background concentrations”), which is crucial when estimating enhancements. Common methods for background selection include using 2-D approximations with spatially adjacent satellite measurements (Li et al., 2023; Qin et al., 2023), extracting data from global models (Yang et al., 2020) or directly obtaining data from observations (Che et al., 2022; Lauvaux et al., 2016). In the case of in situ measurements, the intricacy of background selection is heightened, requiring careful consideration of the CO<sub>2</sub> concentration at the altitude corresponding to the endpoint of the observation's backward trajectory (Sargent et al., 2018). Column measurements with different observation strategies have been proven to effectively minimize background errors, particularly beneficial for larger cities with high pollution levels (Che et al., 2022; J. Chen et al., 2016; Shekhar et al., 2020).

Column measurements are classified as ground- and space-based observations. The Total Carbon Column Observing Network (TCCON) and Collaborative Carbon Column Observing Network (COCCON) are two global initiatives that set the guidelines of ground-based measurements with Fourier transform spectrometers, from which the CO<sub>2</sub> column-averaged dry-air mixing ratio (XCO<sub>2</sub>) are retrieved from their spectral absorption features in the direct solar sunlight. TCCON uses the standard IFS125 HR high-resolution instrument (spectral resolution better than 0.02 cm<sup>-1</sup>), whereas the COCCON strategy relies on the lower resolution EM27/SUN (better than 0.5 cm<sup>-1</sup>) instrument that can deliver XCO<sub>2</sub> measurements with sufficient quality and has the additional advantage of portability (Alberti et al., 2022). Thus, the COCCON network serves as a valuable complement to the existing more stationary TCCON network, offering the possibility for the deployment of dense COCCON networks within urban areas. Field campaign deployment has proven effective in quantifying urban CO<sub>2</sub> emissions as demonstrated in various cities such as Berlin (Hase et al., 2015; Zhao et al., 2019), Paris (Vogel et al., 2019), Indianapolis (Jones et al., 2021), Munich (Dietrich et al., 2021; Reißmann et al., 2022; Zhao et al., 2022), Beijing (Cai et al., 2021; Che et al., 2022), St Petersburg (Ionov et al., 2021), Tokyo (Ohyama et al., 2023), and Madrid (Tu et al., 2022). Simplified methods have been tested, such as employing the mean wind with differential COCCON gradients to infer local emissions (J. Chen et al., 2016; Taquet et al., 2024) or cross-sectional flux method with mobile measurements to determine the source intensity (Luther et al., 2019). A more comprehensive approach involves using an inversion system to update prior urban estimates, particularly suitable for certain sites that account for computational considerations (Che et al., 2022; Jones et al., 2021; Lauvaux et al., 2016; Nalini et al., 2022; Ohyama et al., 2023; Pisso et al., 2019).

The NASA Orbiting Carbon Observatory-3 (OCO-3) mission collected XCO<sub>2</sub> concentrations from May 2019 until November 2023 (Eldering et al., 2019; Taylor et al., 2020). Its innovative feature is to map out CO<sub>2</sub> column measurements over regional spatial-scale emitters like cities or point sources (industries, power plants) using a

targeted observation mode called Snapshot Area Maps (SAMs). OCO-3 SAMs have demonstrated their capability to enhance estimates of FF CO<sub>2</sub> emissions, as validated through synthetic Bayesian experiments conducted over the Los Angeles Basin (Kiel et al., 2021; Roten et al., 2022). Subsequently, Roten et al. (2023) employed Bayesian inversion techniques to analyze real SAMs observations, providing further evidence of its effectiveness in disentangling specific events impacting the CO<sub>2</sub> emissions within the Los Angeles Basin. OCO-3 SAMs also can be used to assess the point CO<sub>2</sub> emissions from power plants, often in conjunction with Gaussian plume models or cross-sectional flux methods (Cusworth et al., 2023; Guo et al., 2023; Hakkarainen et al., 2023; Lin et al., 2023). Nevertheless, factors such as aerosols with undetermined optical or geometry-related properties introduce biases in SAMs observations (Bell et al., 2023). Accurate differentiation of urban-scale XCO<sub>2</sub> signals requires validation through ground-based Fourier transform infrared (FTIR) measurements. Kiel et al. (2021) found a reasonable consistency between TCCON sites (with an Root Mean Square Error (RMSE) of 0.23 ppm) and OCO-3 SAMs over Los Angeles. Zhou et al. (2022) identified a positive XCO<sub>2</sub> difference of 0.92 ppm in the urban area of Beijing and 1.48 ppm in the surrounding countryside through urban-rural EM27/SUN measurements compared to OCO-3 SAMs. A higher error estimate of 1.06 (±1.08) ppm between OCO-3 and a dense FTIR network was found over Mexico City (Che et al., 2024b). The measurements conducted in the tropical African city of Jinja using EM27/SUN indicate a lower estimate of 1.15 (±1.61) ppm for OCO-3 (Humpage et al., 2023). This prompts an exploration into the capability of OCO-3 SAMs as an observational constraint for urban CO<sub>2</sub> emissions. A potential approach is to compare the inversion results from OCO-3 and FTIR for urban areas under various conditions to determine more rigorously the potential of XCO<sub>2</sub> retrievals from space to constrain urban CO<sub>2</sub> emissions.

The Mexico City Metropolitan Area (MCMA) has become the most populous urban region in North America and in the top five megacities worldwide (around 22 million inhabitants as of 2023). To quantify the urban CO<sub>2</sub> emissions in the MCMA, a dense network of FTIR spectrometers, including 6 portable EM27/SUN and 1 IFS120/5 HR instrument were deployed within and around the MCMA. This network aimed to track intra-city gradients in atmospheric column CO<sub>2</sub> concentrations (XCO<sub>2</sub>) from October 2020 to May 2021 as part of the French-Mexican MERCI-CO<sub>2</sub> project, providing a unique opportunity to validate the capability of OCO-3 SAMs in constraining the urban CO<sub>2</sub> emissions. Over these 7 months, 20 XCO<sub>2</sub> images (OCO-3 SAMs) were collected over the MCMA. Che et al. (2024b) revealed that the XCO<sub>2</sub> gradients observed between the urban plume and its surroundings show a good agreement between OCO-3 and the FTIR stations with a Pearson correlation coefficient (*R*) of 0.92, decreasing significantly when comparing intra-city gradients (*R* = 0.24).

In this study, we conducted separate assimilations of two types of dense column-integrated observations (the FTIR network and OCO-3 SAM observations). These assimilations aimed to optimize the estimation of anthropogenic and biogenic CO<sub>2</sub> emissions from the MCMA, with further utilization of FTIR data to evaluate the constraining capability of OCO-3. Section 2 introduces the data utilized in this study along with details on the Lagrangian inversion system. Section 3 presents an analysis and comparison of the posterior results obtained from OCO-3 and FTIR. Finally, Section 4 offers a discussion and summary of this study.

## 2. Lagrangian Inversion Framework

### 2.1. Observed Constraints

Two distinct types of dense column measurements were employed over the MCMA. The first involves daylight column data collected from 7:00 to 18:00 local time in central Mexico, gathered at seven FTIR sites (Figure S1 in Supporting Information S1). The second type comprises SAMs observations from OCO-3 (Figure S2 in Supporting Information S1). A detailed description of this FTIR campaign and data retrieval method is presented in Taquet et al. (2024) and Che et al. (2024b). It is important to note that we used GGG2014 as the prior profiles for EM27/SUN and WACCM as the prior profiles for IFS125HR in the retrieval algorithm. Additionally, we incorporated the latest GGG2020 a priori profiles (Figure S3 in Supporting Information S1) and conducted a sensitivity test using GGG2020. The results, with approximately 1-min intervals for EM27/SUN and approximately 10-min intervals for IFS125HR, are shown in Figure S4 in Supporting Information S1. The bias is less than 0.34 ppm, and when considering hourly analysis, the bias is effectively 0 ppm. Thus, the change to the latest a priori profiles has nearly zero impact on our study. AMEC and ALTZ are sites outside Mexico City in a less populated area and served as background sites, whereas three sites (UNAM and VALL, and BOXO) are well-populated within the urban area. The other two sites (CUAT and TECA) are in peri-urban areas, less impacted by

local emissions. During the seven months of deployment, these instruments have collected a total of 5,228 hourly FTIR observations during the period between October 2021 and May 2022. These data were not evenly distributed spatially or temporally. Figure S1 in Supporting Information S1 illustrates the number of hourly data points for each site used in the FTIR inversion. UNAM, VALL, and AMEC contributed the most to the overall observations (24.2%, 23.1%, and 19.9%, respectively), followed by CUAT, BOXO, TECA, and ALTZ (14.9%, 7.0%, 6.1%, and 4.7%, respectively). Throughout the entire 5,136-hr inversion period, only 1,162 hr recorded observations, as FTIR exclusively operates during cloudless daylight. However, because each observation is influenced by multiple hours of emissions prior to the measurement time (travel time of air masses across the basin), these observations can be used to constrain a larger fraction of the surface fluxes over the observing period. The cumulative influence totaled 4,929 hr, representing nearly 96% of the entire inversion period. For certain time periods, the observational influence is diminished due to the temporal distance of emissions to the observation time, suggesting that our FTIR observations may not effectively constrain CO<sub>2</sub> emissions during these specific times. The measurement cadence of EM27/SUN (nearly 1 min) and IFS 125 HR (nearly 10 min) is high. Consequently, the statistical observed error in the time series of XCO<sub>2</sub> (in Equation 10) could be obtained by comparing the raw time series with a smoothed version calculated using a running mean with a time window of 1 hr. The average observed error for FTIR measurements is 0.25 ppm.

OCO-3 is fixed-mounted on the International Space Station and is equipped with a 2-D pointing mirror assembly that enables scanning larger areas during a single overpass (SAM observation mode) with a sounding area of 80 × 80 km<sup>2</sup> (Bell et al., 2023), which is suitable to detect the intra-urban XCO<sub>2</sub> characteristic (Kiel et al., 2021). The spatial resolution for each pixel size is ~1.29 × 2.25 km<sup>2</sup>. Unlike other sun-synchronous orbit satellites (OCO-2, GOSAT, TanSat, etc.), OCO-3 undertakes a non-sun-synchronous orbit, so OCO-3 does not overpass over a specific city at a fixed time. We used OCO-3 level 2 bias-corrected XCO<sub>2</sub> data (version 10.4r) generated by the Atmospheric CO<sub>2</sub> Observations from Space (ACOS) algorithm (Taylor et al., 2023). MCMA was likely to be selected as an OCO-3 SAM-targeted region thanks to the absence of other hot spots along the track, allowing for the Mexico City plume to be easily detectable. Figure S2 in Supporting Information S1 shows all the 20 OCO-3 SAMs images collected over MCMA of sufficiently high-quality (*xco2\_quality\_flag* = 0) during our study period. A distinct urban signal from MCMA is evident in these fine-spatial XCO<sub>2</sub> maps. As mentioned earlier, the OCO-3 overpass times in MCMA vary, ranging from 10:00 to 15:00 (local time). The measurement errors of OCO-3, considering its high spatial resolution, were calculated using a spatial 10 km circle smoothing mean, resulting in an averaged observed error of 0.7 ppm for OCO-3, approximately two times higher than that of the FTIR data set. In the inversion process, only OCO-3 data within MCMA is utilized. The number of individual soundings utilized in each day ranges from 62 to 858. Data on April 20<sup>th</sup>, 2021 is not used in the inversion due to the low data availability (fewer than 10 high-quality soundings) over MCMA.

## 2.2. Forward Lagrangian Transport Model

The X-Stochastic Time-Inverted Lagrangian Transport (X-STILT) model (D. Wu et al., 2018) driven by the Weather Research and Forecasting (WRF) at 1-km resolution was used here to relate our atmospheric observations to surface fluxes and background conditions. The configuration in WRF and X-STILT are detailed and evaluated in Xu (2023) and Che et al. (2024b). WRF model performance was evaluated using meteorological surface stations across the MCMA region for wind speed and direction (with errors ranging from -0.36 to -0.72 m/s) and planetary boundary layer (PBL) height using a lidar at the UNMA site south of MCMA (afternoon errors from -550 to 110 m). Detailed evaluation is provided in Xu (2023). WRF winds are used to drive an ensemble of particles in backward trajectories, which are released and traced 24 hr backwards in time from each of the seven site locations for all observed hours. In the forward process, simulated XCO<sub>2</sub> ( $XCO_{2, sim}$ , unit of ppm) are the sum of prior FF emissions ( $s_{p, ff}$ , in units of  $\mu\text{mol}/\text{m}^2\text{s}$ ) and biogenic emissions ( $s_{p, bio}$ , in units of  $\mu\text{mol}/\text{m}^2\text{s}$ ) enhancements, combined with the background values ( $z_{back}$ , in units of ppm, representing every contribution from outside the MCMA domain).

$$XCO_{2, sim} = H_s \times s_{p, ff} + H_s \times s_{p, bio} + H_b \times z_{back} \quad (1)$$

Column footprint ( $H_s$ , in unit of  $\text{ppm}/\mu\text{mol}/\text{m}^2\text{s}$ ) is a function of backward time and location for each observation. It is used to transform emissions into XCO<sub>2</sub> enhancements, as shown in Figure 1. The integrated area overlap measurement index (IAOMI), as described by Yadav et al. (2023), quantifies the overlap and shared information



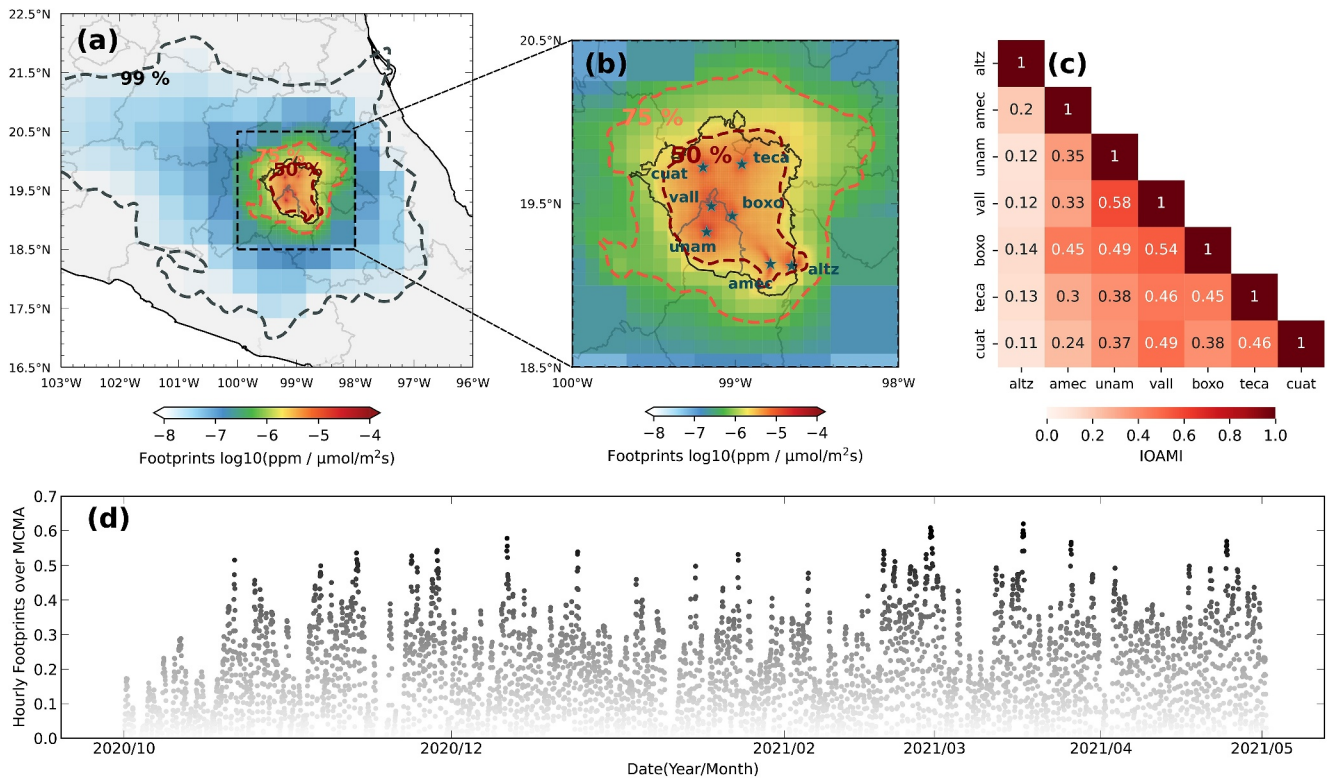


**Figure 1.** Averaged footprints for all sites during study period with footprint contours of its 50, 75, and 99 percentile level shown over (a) central Mexico and (b) Mexico City Metropolitan Area (MCMA). Note the Log10 scale as footprint very quickly decreases away from the observation location. Seven sites used in this study are marked with stars in deep teal color. (c) Integrated Area Overlap Measurement Index to demonstrate similarity between footprints at different Sites. (d) Cumulative footprints over MCMA on the whole campaign period on an hourly basis.

between two observations by calculating their common contributions, serving as a tool for understanding the uniqueness and similarity in observations data, analyzed in terms of spatial-temporal intensity and used to describe the footprint overlap of different sites ( $F$  for site 1 and  $G$  for site 2 as an example), with its methodology akin to a Venn diagram (Equation 2) and will be analyzed in Section 3.1.

$$V_{F, G} = \frac{\sum_{A_F \cup A_G} \min(F, G)}{\sum_{A_F \cup A_G} \max(F, G)} \quad (2)$$

Where  $A_F$  (or  $A_G$ ) represents the set of values for which the forward operator  $F$  (or  $G$ ) produces positive outcomes. The footprint for background ( $H_b$ ,  $n_{time} \times n_{obs}$ , dimensionless quantity) differs from the footprint for emissions ( $H_s$ ,  $n_{time} \times n_{obs} \times n_{land}$ ).  $H_b$  only has a temporal dimension and is utilized to transform background values over the entire inversion time period (dimension is:  $n_{time}$ ) to the background extracted time (dimension is:  $n_{obs}$ ).  $z_{back}$  is the integrated column extracted from CAMS (version: v21r2). This extraction is based on backward trajectories from X-STILT and the averaging kernel derived from column measurements, and the detailed background extraction method is outlined in Che et al. (2024b). Given that background values either account for the spatial pattern or introduce no bias ( $0 \pm 0.09$  ppm in Figure S3 in Supporting Information S1), we only consider their time variations.

Prior anthropogenic  $\text{CO}_2$  emissions at 1 km ( $s_{p, ff}$ ) are from a Mexico-specific inventory UNAM\_EMI and the global inventory ODIAC (Open-source Data Inventory for Atmospheric Carbon dioxide) (Oda et al., 2018). These two inventories exhibit significant discrepancies over MCMA (approximately 40%), with UNAM\_EMI providing more detailed information on point sources across our inversion domain (see Figure 2). High-resolution prior biogenic  $\text{CO}_2$  emissions ( $s_{p, bio}$ ) were from the ecological model CASA (Carnegie-Ames-Stanford Approach). Biogenic emissions are zero over urban areas and distributed more evenly outside the urban areas (Figures 2a and 2e). Moreover, we simply define the urban boundary as the region with zero biogenic emissions.

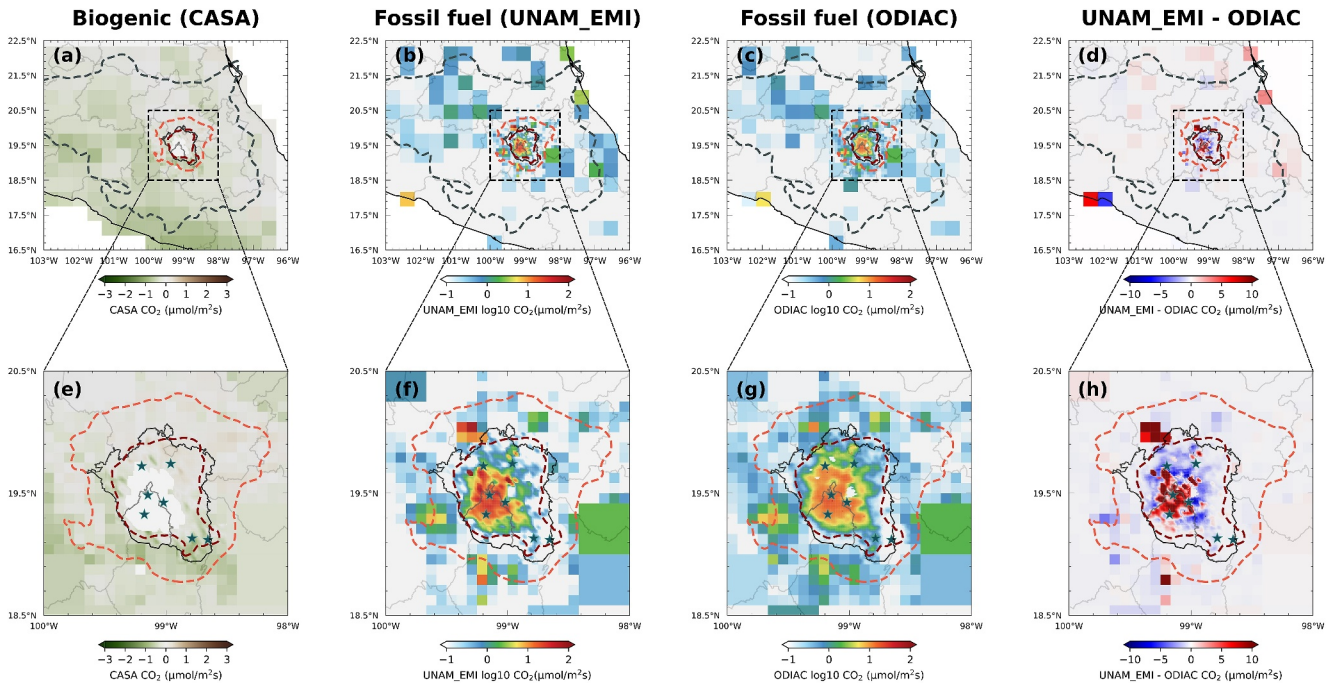


**Figure 2.** (a, e) Map of biogenic CO<sub>2</sub> emissions (μmol/m<sup>2</sup>s) from CASA. Maps of fossil fuel CO<sub>2</sub> emissions (log<sub>10</sub> (μmol/m<sup>2</sup>s)) from UNAM\_EMI (b, f) and ODIAC (c, g). The differences of UNAM\_EMI and ODIAC are also shown in panels (d, h). The Mexico City Metropolitan Area is indicated with black line. Footprint contours are also shown in each figure with 50% and 75% percentile.

For detailed information on prior inventories and prior background values, refer to Che et al. (2024b). All these linear operators in Equation 1 are combined into Jacobian ( $H$ ) and all the prior information are grouped into one vector ( $s_p$ ), which can be used in the inversion system. The  $H_s$  matrix comprises elements represented as ( $n_{time} \times n_{obs} \times n_{land}$ ), where  $n_{time}$  denotes all inversion time,  $n_{obs}$  signifies the total number of observations, and  $n_{land}$  encompasses all spatial points. On the other hand, the  $H_b$  matrix is solely composed of an  $n_{time}$ -dimensional vector. As for  $s_{p, ff}$  and  $s_{p, bio}$ , each consists of a ( $n_{time} \times n_{land}$ )-dimensional structure. Meanwhile,  $z_{back}$  is uniquely characterized by an  $n_{time}$ -dimensional configuration.

$$H = [H_s \quad H_s \quad H_b] \quad (3)$$

$$s_p = \begin{bmatrix} s_{p, ff} \\ s_{p, bio} \\ z_{back} \end{bmatrix} \quad (4)$$

As mentioned in Section 2.1, for FTIR,  $n_{time}$  is set to 5,136 and  $n_{obs}$  is 5,228. However, for satellite data, due to the substantial time gap between each overpass, we perform independent inversion for each overpass. Regarding  $n_{land}$ , two inversion schemes are considered and will be discussed in Section 3.1. The primary configuration involves considering the spatial grid within MCMA with a 1-km spatial resolution, resulting in  $n_{land} = 9,751$ . Another configuration is for the entire grid (the entire central Mexico region, which includes the total 99% footprint region shown in Figure 1a), but opting for an inversion across the entire area with a 1 km resolution would result in over 25,000 grids, leading to a substantial spatial error covariance matrix (will be introduced in the next Section). To address this, we adopted the un-gridded technique utilized in previous studies such as L. Wu et al. (2011) and Gómez-Ortiz et al. (2023). This technique involves setting a fine resolution near the observation sites (1 km) and a coarser resolution in the outer regions (10, 50 km) (will be introduced in the first paragraph of Section 3.1). The spatial grid for the entire inversion was reduced to 10,877 through the implementation of a multi-resolution grid scheme.

### 2.3. Bayesian Inversion Model

Our analytical inversion framework computes algebraic solutions for the linear Gaussian Bayesian problem but faces limitations due to memory constraints arising from the construction of large spatial and temporal covariance matrices, particularly when aiming to enhance spatial-temporal resolution in the inversion process. To address challenges associated with these matrices, various ensemble methods provide approximate solutions for the analytical approach (e.g., H. W. Chen et al. (2023)). In dealing with large temporal matrices, some studies adopt the practice of using the current time period as the prior for the next, although this method tends to introduce discontinuities in results and encounters difficulties in capturing temporal correlations at nodal points. Additionally, the variational method proves effective for addressing nonlinear problems; however, it is limited in its ability to offer accurate posterior uncertainty and is associated with elevated computational expenses. Some studies seek to improve uncertainty estimation in variational methods through ensemble approaches, thereby further increasing computational demands for inversion research (Desroziers et al., 2016). This study presents a novel approach that employs a multi-node parallel strategy to tackle the computational challenges associated with analytical methods to some extent for high spatial and temporal estimation of CO<sub>2</sub> emissions in urban studies. The proposed approach leverages 120 nodes to efficiently process the expansive matrix. Additionally, these matrices can be temporarily stored as sparse matrices to reduce storage requirements.

An analytical inversion model spanning from October 2020 to May 2021 was implemented to robustly derive posterior estimates  $s$  encompassing FF and biogenic components at 1-km and 1-hr resolutions ( $s_{ff}$ ,  $s_{bio}$ ) with dimension of  $n_{time} \times n_{land}$ . Additionally, background posterior values at a 1-hr resolution ( $z_{back}$ ) over the MCMA were also updated.  $V_s$  represents the posterior covariance for  $s$ .

$$\hat{s} = s_p + (HQ)^T (HQH^T + R)^{-1} (z - Hs_p) \quad (5)$$

$$V_{\hat{s}} = Q - (HQ)^T (HQH^T + R)^{-1} HQ \quad (6)$$

An advantage of the analytical inversion method is that it allows us to evaluate the inversion performance using the averaging kernel and error reduction (ER). Error reduction (ER) is the relative reduction of posterior uncertainty ( $\sigma_V$ ) compared to prior uncertainty ( $\sigma_Q$ ). The averaging kernel ( $A$ ) indicates the sensitivity of the posterior results to the true state and is used to assess the spatial structure of inverse flux estimates. It is calculated using the Kalman gain ( $G$ ) with  $H$ . The degrees of freedom for signal (DOFS) is the trace of  $A$  and describes the amount of independent information that can be obtained from the observations.

$$ER = \left(1 - \frac{\sigma_V}{\sigma_Q}\right) \times 100\% \quad (7)$$

$$A = GH, G = (HQ)^T (HQH^T + R)^{-1} \quad (8)$$

For each component of  $Q$ , it is structured as the prior error variance ( $\sigma_s^2$ ) and the Kronecker product of temporal covariance ( $D$ ) and spatial covariance ( $E$ ) following the methodology proposed by Yadav and Michalak (2013). It is important to note that we only consider  $D$  in the background component, while both  $D$  and  $E$  are considered for the FF and biogenic components.

$$Q = \begin{bmatrix} Q_{ff} & 0 & 0 \\ 0 & Q_{bio} & 0 \\ 0 & 0 & Q_{back} \end{bmatrix} \quad (9)$$

$$Q = \sigma_s^2 D \otimes E \quad (10)$$

where  $\sigma_s$  is a time-space varying element assumed to have a linear relationship with prior emissions:

$$\sigma_s = bs_p + c \quad (11)$$

**Table 1**  
Sensitivity Test Results for Inversion Analysis

Parameter	Long name	Sensitivity test
$l_{s, ff}$	Spatial error correlation length for prior fossil fuel emissions	1, 4, 8, <b>12*</b> , 20, 40 km
$l_{s, bio}$	Spatial error correlation length for prior biogenic emissions	2, 8, 16, <b>24*</b> , 40, 60 km
$l_{\tau, ff}$	Temporal error correlation length for prior fossil fuel emissions	0, <b>1*</b> , 3, 5, 10 days
$l_{\tau, bio}$	Temporal error correlation length for prior biogenic emissions	0, 1, <b>2*</b> , 6, 10 days
$l_{\tau, back}$	Temporal error correlation length for prior background values	0, 1.5, <b>3*</b> , 9, 15 days
$b_{ff}$	Uncertainty of prior fossil fuel emissions	0.2, <b>0.8*</b> , 1.5, $3 \times 100$ %
$b_{bio}$	Uncertainty of prior biogenic emissions	0.4, <b>1.6*</b> , 3, $6 \times 100$ %
$R_{trans, percent}$	Transport error	<b>0.2*</b> , 0.5, 1, 2, $3 \times 100$ %

Note. Baseline Values Marked with an Asterisk (\*).

For the FF and biogenic components,  $c$  is set to 0 for simplicity. Concerning the background error component, a comparison was conducted between the simulated background from CAMS and the observed values from background sites (AMEC and ALTZ). A fitting slope near unity was identified for both FTIR and OCO-3, with biases of 1.34 and 0.11 ppm, respectively (Che et al., 2024b). Consequently, we set  $b$  to 0, and  $c$  was assigned the determined bias for the background part.  $D$  and  $E$  are defined using exponential decay equations.

$$E = e^{-\frac{X_s}{l_s}} \quad (12)$$

$$D = e^{-\frac{X_t}{l_t}} \otimes e^{-\frac{X_{t, intra}}{l_{t, intra}}} \quad (13)$$

where  $X_t$  and  $X_s$  are the separation distances between the estimated locations in time and space,  $l_t$  and  $l_s$  are the corresponding correlation range parameters. As for the temporal correlation, we account for both daily correlation and intradiel correlation of 3 hr, as suggested in Wesloh et al. (2020). Each component is defined by an exponential correlation function (refer to Equations 12 and 13). Figure S5 in Supporting Information S1 provides an illustrative example of the temporal correlation decay function.

$$R = R_{obs} + R_{trans} \quad (14)$$

where  $R_{obs}$  is the error stemming from the XCO<sub>2</sub> observations (introduced in Section 3.1).  $R_{trans}$  is the error from the transport model. Due to the absence of an adequate meteorological data set to assess the transport error, we determined it as a linear multiple of the simulated XCO<sub>2</sub> enhancements (Zheng et al., 2019). This approach introduces error, and we subsequently discuss its influence on the final posterior estimates (see Section 3.2). Estimating the appropriate parameters in  $Q$  and  $R$  poses a significant challenge, with no universally recognized approach for this problem. These parameters are determined either through empirical experience (Lauvaux et al., 2016) or based on eddy-flux measurements (Chevallier et al., 2012). In this study, we perform comprehensive sensitivity analyses on all relevant parameters to assess their impact on the inversion results.

The chi-square statistic ( $\chi^2$ ) is a metric used to assess the consistency between prescribed error parameters and the prior model-data mismatch (Kaminski et al., 2001). Note that this condition ( $\chi^2 = 1$ ) is sufficient but not necessary to define the parameter performance.

$$\chi^2 = \frac{1}{n}(y - Hs_p)^T (HQH^T + R)(y - Hs_p) \quad (15)$$

Yadav et al. (2023) proposed a method based on the analysis of derivatives for various variables to determine the most influential parameters in the inversion system. In our case, where the state vector and covariance matrix here is a large matrix, the use of derivative equations is not suitable. Instead, we conducted a discrete value analysis of derivatives. All undetermined parameters in the inversion system, along with their respective explanations, are summarized in Table 1. The bold numbers with small asterisks represent the values in our baseline configuration



**Table 2**  
*XCO<sub>2</sub> Enhancements and Its Percentage Over Mexico City Metropolitan Area Compared to the Whole Central Mexico for Each Site*

Site name	Simulated $\Delta XCO_{2, ff}$ UNAM_EMI(MCMA percentage)	Simulated $\Delta XCO_{2, ff}$ ODIAC(MCMA percentage)	Simulated $\Delta XCO_{2, bio}$ CASA(MCMA percentage)
CUAT	0.02 ~ 3.79 ppm(73.21%)	0.03 ~ 2.31 ppm(81.28%)	-0.51 ~ 0.54 ppm(87.19%)
TECA	0.01 ~ 1.99 ppm(73.58%)	0.01 ~ 1.54 ppm(76.32%)	-0.35 ~ 1.22 ppm(51.65%)
UNAM	0.08 ~ 7.16 ppm(95.33%)	0.09 ~ 4.85 ppm(95.52%)	-0.45 ~ 1.01 ppm(50.21%)
VALL	0.20 ~ 4.83 ppm(94.21%)	0.17 ~ 3.67 ppm(94.53%)	-0.50 ~ 1.02 ppm(35.22%)
BOXO	0.03 ~ 3.48 ppm(92.26%)	0.05 ~ 3.13 ppm(93.42%)	-0.33 ~ 0.44 ppm(30.22%)
AMEC	0 ~ 2.04 ppm(68.03%)	0 ~ 1.81 ppm(72.54%)	-1.19 ~ 1.57 ppm(64.85%)
ALTZ	0 ~ 0.45 ppm(34.02%)	0 ~ 0.40 ppm(22.82%)	-0.54 ~ 0.02 ppm(38.20%)

used in the control experiment to explore posterior feedback for each parameter. Detailed sensitivity results will be discussed in Section 3.2.

### 3. Results

#### 3.1. Selection of the Inversion Region

To estimate urban-scale CO<sub>2</sub> emissions, it is essential to identify the regions that exert the greatest influence on our seven observation sites, in other words, the regions that our observations can constrain (Shan et al., 2019). Footprints represent the correction potential of the inversion, indicating that column measurements can only correct emissions at specific times and region. Utilizing our footprints to determine which region plays a predominant role in influencing the observations is a reliable approach (Che et al., 2022). Figure 1 displays the footprints of seven sites, with contours at 50%, 75%, and 99% of the footprint sum values. The aggregated footprints from these 7 FTIR sites reveal that the 50% influence area is primarily within the MCMA, surrounded by high mountains able to trap pollution within the basin. The largest footprint (99%) is mainly located in the center of Mexico (Figures 1a and 1b). The 99%-footprint region is presented at a 50-km scale, the 75%-footprint region at a 10-km scale, and the inner MCMA region (which is of particular interest) at a 1-km scale. This multi-spatial setting reduces the number of unknowns and compared to a full 1-km scale region, and the aggregation has a negligible effect on the simulation (Figure S6 in Supporting Information S1). Footprints from different sites can overlap, hence the IAOMI (introduced in Section 2.2) can be used to quantify the shared intensity content between footprints at different sites (Yadav et al., 2023). We employed this index to assess the degree of connection across all the footprints from the different sites (Figure 1c). The ALTZ site shows less connectivity with the other sites due to its high altitude, as ALTZ is often located above the PBL height of the basin. Three urban sites (UNAM, VALL, and BOXO) exhibit a stronger connectivity with each other and the most connectivity with the other sites, given their central locations within the MCMA. Examining the time series of footprints over MCMA (Figure 1d) reveals that these footprints are not evenly distributed on an hourly basis.

Figure 2 presents all the emission inventories utilized in this study, including FF emissions from UNAM\_EMI and ODIAC and biogenic emissions from CASA. Building upon our earlier work (Che et al., 2024b), we note site-specific variations in FF and biogenic CO<sub>2</sub> emissions: urban sites (UNAM, VALL, and BOXO) exhibit a predominant FF signature, comprising over 90% of the total contribution from FF and biogenic emissions; inflow sites (CUAT and TECA) display FF signals at approximately 60 ~ 70%, whereas background sites, especially ALTZ, demonstrate significant biogenic contributions, with 78% of the XCO<sub>2</sub> enhancements at this site originating from biogenic fluxes. Table 2 provides a summary of simulated FF and biogenic XCO<sub>2</sub> enhancements from these inventories across the entire footprint area and within MCMA. Simulated FF XCO<sub>2</sub> enhancements from UNAM\_EMI and ODIAC over the entire footprint range 0–7.16 ppm and 0–4.85 ppm, respectively. Over MCMA, these enhancements account for around 84% and 86% of the total, respectively. Within MCMA, biogenic enhancements range from -1.19 to 1.57 ppm, constituting 49.5% of the total biogenic fluxes (-1.4 to 2.0 ppm). Urban and nonurban sites exhibit distinct emission characteristics. For the three urban sites (UNAM, VALL, and BOXO), 92–94% of FF XCO<sub>2</sub> enhancements from UNAM\_EMI and ODIAC occur within MCMA. Conversely, CUAT, TECA, and AMEC show FF accounting for approximately 70%, and ALTZ presents a more complex scenario, with the FF signal originating within MCMA accounting for only 34%. Although FF emissions exhibit a

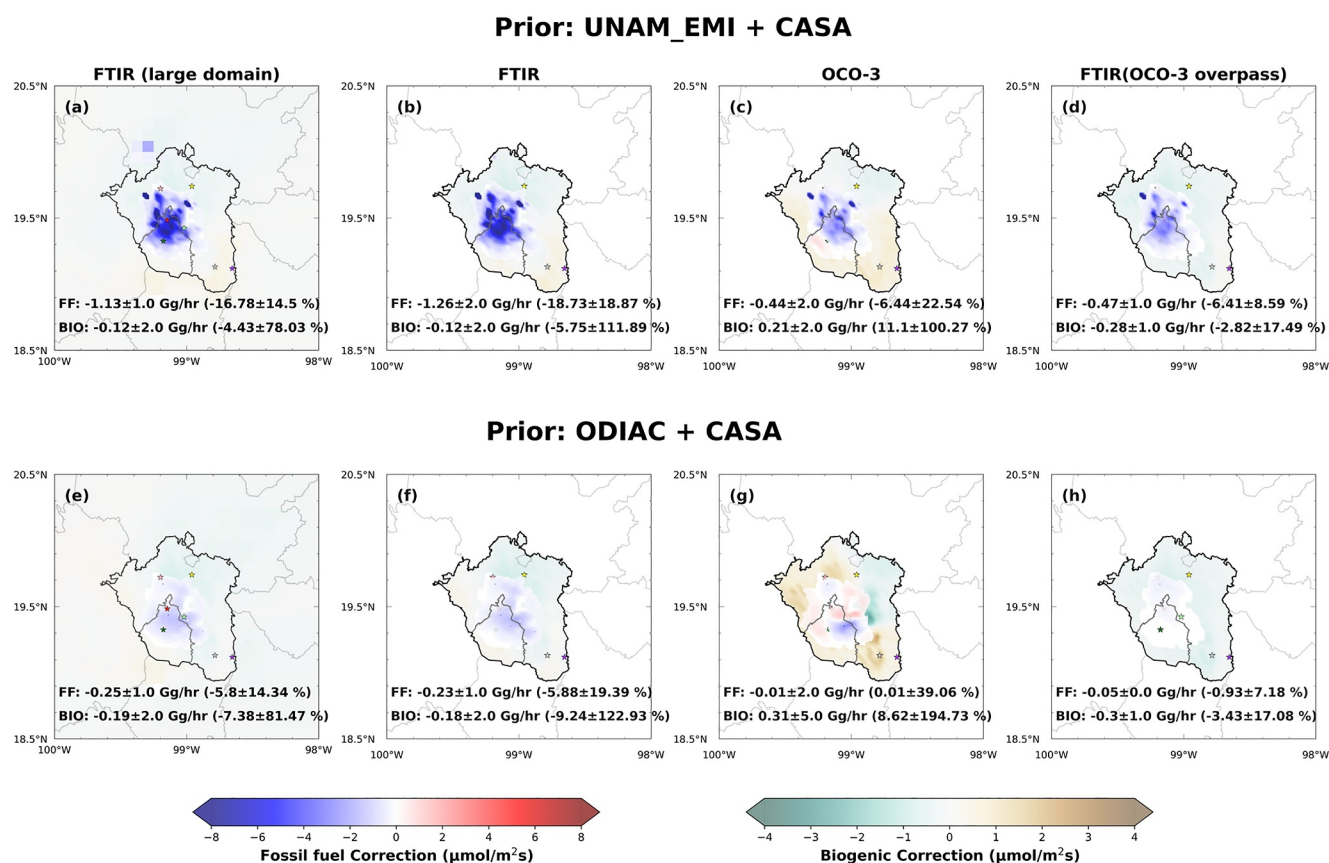


**Figure 3.** Map of the difference in anthropogenic and biogenic CO<sub>2</sub> emissions ( $\mu\text{mol}/\text{m}^2\text{s}$ ) between posterior and prior estimates. The posterior estimates are constrained with Fourier transform infrared (FTIR) using large domain inversion region settings (first column) and Mexico City Metropolitan Area inversion settings using observations from FTIR, OCO-3, and FTIR during OCO-3 overpass time (second to fourth columns, respectively). Panels (a–d) use prior estimates from UNAM\_EMI and CASA, whereas panels (e–h) use prior estimates from ODIAC and CASA. The blue-red colorbar represents anthropogenic corrections, and the green-brown colorbar represents biogenic corrections. The correction values in the lower left part of each subplot represent the average and one standard deviation of the hourly differences between spatially aggregated posterior and prior emissions for fossil fuel and biogenic (BIO) sources. The percentages in parentheses indicate the average and one standard deviation of the correction percentages.

strong signal over MCMA, biogenic emissions are more evenly distributed outside the urban areas. Despite the limited footprint outside MCMA, suggesting potential inaccuracies in representing this outside region, the addition of this area would incur additional computational costs. Thus, a delicate balance between computational costs and the accuracy of posterior corrections must be maintained. As a result, it is imperative to assess the signals outside MCMA and quantify their significance on the inversion results.

Two tests were conducted for MCMA-only inversion, and an additional test focused on the inversion for the whole region (the entire central Mexico region, which included the whole footprint area) (Introduced in Section 2.2). We utilized the basic configuration outlined in Table 1 for both tests. The comparison of the posterior correction for these two schemes is presented in Figures 3a and 3e and S 7–8. It is worth noting that the primary adjustment region remains within MCMA. As corrections in the outermost regions were almost negligible, we illustrate the corrections around the 75% footprint region in Figures 3a and 3e. The comparison of inversion results between MCMA-only and whole region (shown in Figure 1a) inversion reveals few differences. Specifically, for UNAM\_EMI, the CO<sub>2</sub> corrections for emissions coming within MCMA are  $-1.26 \pm 2.0 \text{ GgCO}_2/\text{hr}$  ( $-18.73 \pm 18.87\%$ ) and  $-1.13 \pm 1.0 \text{ GgCO}_2/\text{hr}$  ( $-16.78 \pm 14.5\%$ ) for the two inversion schemes, respectively. Simultaneously, CASA has been corrected by  $-0.12 \pm 2.0 \text{ GgCO}_2/\text{hr}$  ( $-5.75 \pm 111.89\%$ ) and  $-0.12 \pm 2.0 \text{ GgCO}_2/\text{hr}$  ( $-4.43 \pm 78.03\%$ ) within MCMA for the two inversion schemes. In the case of ODIAC, the posterior correction is  $-0.23 \pm 1.0 \text{ GgCO}_2/\text{hr}$  ( $-5.88 \pm 19.39\%$ ) and  $-0.25 \pm 1.0 \text{ GgCO}_2/\text{hr}$  ( $-5.8 \pm 14.34\%$ ), while the biogenic component from CASA corrects by  $-0.18 \pm 2.0 \text{ GgCO}_2/\text{hr}$  ( $-9.24 \pm 122.93\%$ ), and  $-0.19 \pm 2.0 \text{ GgCO}_2/\text{hr}$  ( $-7.38 \pm 81.47\%$ ), respectively. The fossil-fuel correction for UNAM\_EMI shows a larger value

compared to ODIAC. The primary reason is that UNAM\_EMI assigns higher values at the Tula power plant and industrial complex, located to the north-east outside the MCMA. Specifically, when correcting emissions from only within MCMA, the correction over the power station compensates within MCMA, potentially leading to exacerbate the underestimation of FF emissions within MCMA. Nevertheless, the area located outside of MCMA still exhibits a slight difference compared to the correction over MCMA, attributable to smaller footprints. The substantial correction outside MCMA requires a slight adjustment over MCMA. The comparison of UNAM\_EMI and ODIAC reveals different patterns in anthropogenic and biogenic CO<sub>2</sub> emissions distribution. The direct comparison of the posterior emissions from UNAM\_EMI and ODIAC will be discussed in the next section. In this section, the primary focus remains on discussing how big the area we need for inversion. Regarding the temporal scale of this comparison, the whole MCMA correction for these two schemes and the comparison figures are presented in Figure 3 and Figures S7–S8 in Supporting Information S1. It can be observed that the posterior correction in temporal scale are very similar for these two schemes, with some differences that vary along with the signals.

### 3.2. Inversion Results for FTIR

In the preceding section, external contributions (outside MCMA) is approximately 0.13 Gg/hr for the FF component from UNAM\_EMI and 0.02 GgCO<sub>2</sub>/hr from ODIAC, with the contribution from biogenic sources being nearly negligible. Hence, given the close alignment in corrections for MCMA in both schemes and in an effort to reduce computational expenses, we specifically selected MCMA as the sole focus for our inversion study. As the result reached in the previous section, the posterior FF CO<sub>2</sub> emissions over MCMA showed a reduction, resulting in an 18.73 ± 18.87% overestimation for UNAM\_EMI (1.26 ± 2.0 Gg CO<sub>2</sub>/hr) and a 5.88 ± 19.39% overestimation for ODIAC (0.23 ± 1.0 Gg CO<sub>2</sub>/hr). This reduction was particularly pronounced for the urban area (defined in Section 2.2), showing a 20.6% overestimation for UNAM\_EMI (1.11 Gg CO<sub>2</sub>/hr) and a 6.1% overestimation for ODIAC (−0.21 Gg CO<sub>2</sub>/hr), respectively. Corrections for the biogenic component were relatively minor, resulting in a decrease of 0.12 ~0.18 Gg CO<sub>2</sub>/hr (around 5.75 ~9.24% correction). Although the one standard deviation of correction percentages were substantial (even larger than 100%), this was primarily due to the small prior values associated with the biogenic component.

Three commonly employed metrics to assess the effectiveness of our inversion process are (a) a comparison with observations, (b) the calculation of averaging kernel, ER, and (c) sensitivity tests of the parameters (Lu et al., 2020; van der Velde et al., 2021; Yadav et al., 2023). In this study, our focus is on comparing the relative values of XCO<sub>2</sub> enhancements (ΔXCO<sub>2</sub>, XCO<sub>2</sub> observed by each site against corrected CAMS background values) rather than the absolute values. This choice stems from the realization that absolute value comparisons are largely influenced by the simulation of background values. Our primary interest lies in evaluating the correction part of our emissions, leading us to assess ΔXCO<sub>2</sub> rather than XCO<sub>2</sub>. The evaluation of ΔXCO<sub>2</sub>, based on prior (hollow triangle) and posterior estimates (filled triangle), with respect to the observations, is presented in a scatter plot (Figures 4a and 4b and Tables S1 and S2 in Supporting Information S1). RMSE, correlation coefficient (*R*) and the linear fitting slope serve as three metrics aimed at comparing simulated XCO<sub>2</sub> enhancements with observed ΔXCO<sub>2</sub> from FTIR measurements. Considering the entire FTIR data set, *R* based on prior estimates ranges from 0.58 to 0.62 and significantly improves to 0.92–0.95 with posterior estimates. Different sites exhibit varying degrees of improvement. When UNAM\_EMI serves as the prior, *R* for three urban sites (UNAM, VALL, and BOXO) ranges from 0.31 to 0.53 and from 0.22 to 0.51 when ODIAC is the prior. The two suburban sites (CUAT and TECA) have *R* ranging from 0.43 to 0.48 based on UNAM\_EMI as the prior and from 0.38 to 0.43 based on ODIAC as the prior. The worst performance is observed at the two background sites (AMEC and ALTZ), with *R* ranging from −0.2 to 0.18 for UNAM\_EMI and −0.22 to 0.16 for ODIAC. Regarding the posterior results, *R* for all sites improves to 0.87–0.93 for UNAM\_EMI and 0.82 to 0.93 for ODIAC. The enhanced correlation coefficient suggests that the general spatial pattern of CO<sub>2</sub> concentration enhancements is better captured by the inventories after optimization.

As for the overall RMSE metric based on prior estimates, it is 0.97 ppm for UNAM\_EMI and 0.88 ppm for ODIAC. These values improve to 0.28 and 0.32 ppm, respectively, in the posterior. Different sites exhibit distinct results; RMSE based on UNAM\_EMI is 0.97–1.13 ppm for three urban sites, 0.61–0.78 ppm for two suburban sites, 0.87 ppm for AMEC, and 0.56 ppm for ALTZ. As for ODIAC, RMSE for the three urban sites is 0.92–0.99 ppm, 0.60–0.73 ppm for two suburban sites, 0.88 ppm for AMEC, and 0.56 ppm for ALTZ. Concerning the posterior results for the different sites, RMSE improves to 0.08–0.30 ppm for UNAM\_EMI and 0.08–0.42 ppm

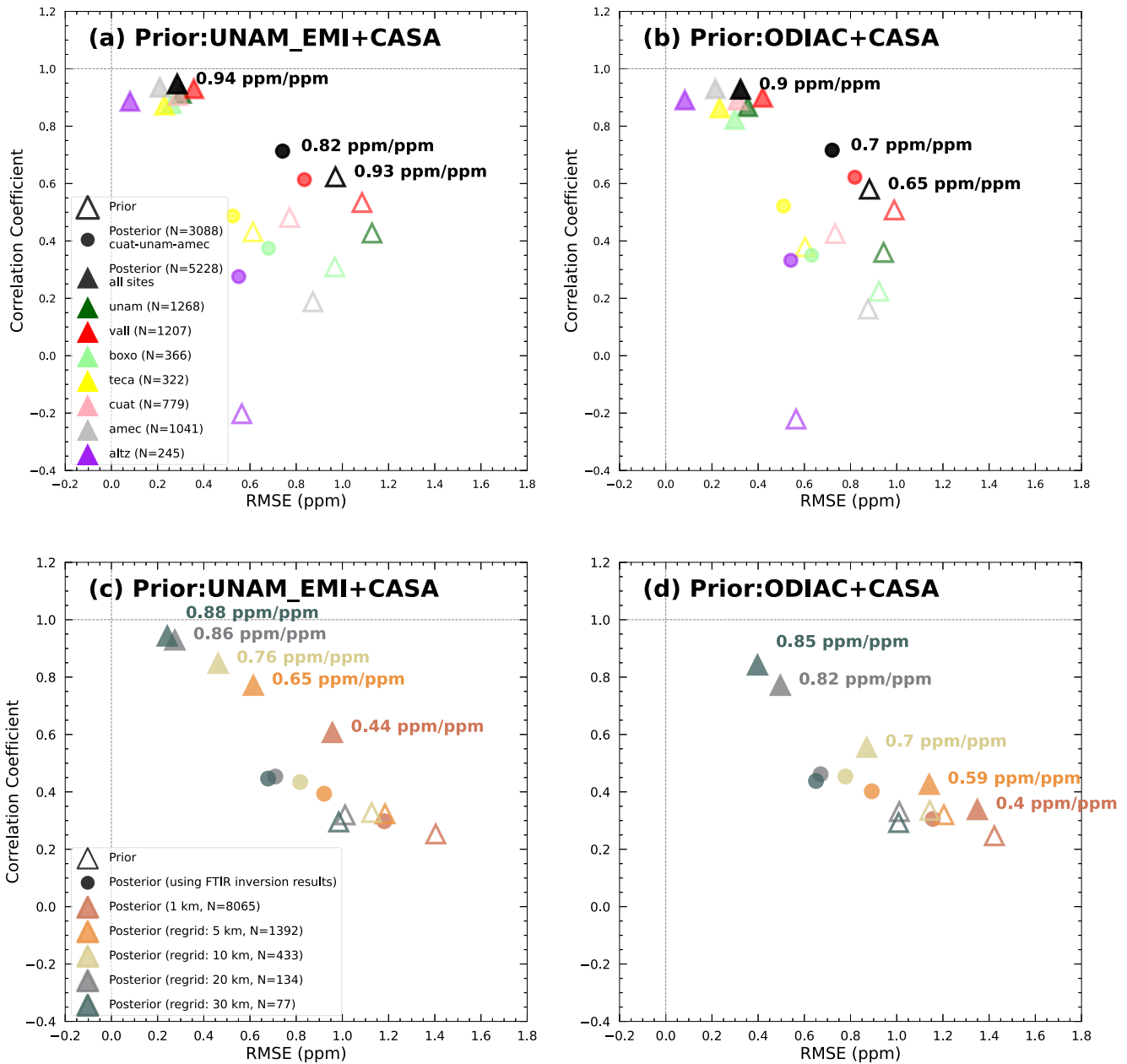


**Figure 4.** Comparison of the simulated XCO<sub>2</sub> enhancements based on prior inventories (open triangles) and posterior results (a, c) using prior inventories from UNAM\_EMI and CASA; and (b, d) using prior inventories from ODIAC and CASA with observed values (filled triangles). Independent evaluations are shown in filled circles. The x-axis represents the root mean square error, and the y-axis represents the correlation coefficient between simulations and observations. Panels (a–b) show the results with Fourier transform infrared, with different colors indicating different sites, whereas panels (c–d) show the results with OCO-3, with different colors indicating different aggregation resolutions.

for ODIAC. The reduction in RMSE indicates significant adjustments in the absolute magnitude of emissions after optimization. Regarding the linear fitting slope displayed on the right side of each triangle, we observe a slight improvement in UNAM\_EMI (from 0.93 ppm ppm<sup>-1</sup> to 0.94 ppm ppm<sup>-1</sup>), whereas ODIAC shows a more substantial improvement (from 0.65 ppm ppm<sup>-1</sup> to 0.9 ppm ppm<sup>-1</sup>). It is worth noting that achieving higher R and lower RMSE brings the slope closer to unity. Note that the prior results may appear slightly different from those presented in the last paper (Che et al., 2024b). This discrepancy arises because, to simplify the problem, we only consider CAMS in the time dimension and do not incorporate its spatial pattern. Whether include the spatial pattern of CAMS does not exert a substantial influence on the obtained outcomes (see Figure S9 in Supporting



Information S1). It is plausible that, for a global coarse model such as CAMS, the minimal spatial gradients around a single city may not be particularly significant. From the comparison of simulated enhancements between observed values, it is evident that posterior results are more robust, significantly improving the degree of alignment with observations. UNAM\_EMI exhibits superior performance in both prior and posterior results compared to ODIAC when using the same covariance parameters.

Additionally, we aimed to investigate whether utilizing a subset of the FTIR observations could improve our simulation performances at other sites (cross-validation). We strategically selected one site from the inflow region (CUAT), one in the urban area (UNAM), and another in the background area (AMEC). These chosen sites have a higher number of observations compared to others (Figure S1 in Supporting Information S1), providing a larger number of simultaneous observations aligned with our validation data sets (TECA, VALL, BOXO, and ALTZ). In total, we gathered 3,088 observations from these three sites. The posterior results for the remaining four sites are presented in Figure 4 (Solid triangle pointing to the left) and Tables S1 and S2 in Supporting Information S1. For the overall set of these four sites, R increased from 0.67 (prior of these four sites) to 0.71 for UNAM\_EMI (a 12.34% improvement compared to the prior simulated results using the whole data set) and from 0.64 to 0.71 for ODIAC (a 20.11% improvement). The RMSE decreased from 0.96 to 0.74 ppm for UNAM\_EMI (a 31.88% reduction) and from 0.89 to 0.72 ppm for ODIAC (a 30.48% reduction). Considering the other sites such as TECA, specifically when using UNAM\_EMI, R improved from 0.43 to 0.49 and from 0.38 to 0.52 for ODIAC. The corrective component contributed to a significant enhancement of 13.6%–29.2% compared to the inversion scheme utilizing the entire FTIR data set. In the case of VALL, R improved from 0.53 to 0.61 based on UNAM\_EMI and from 0.50 to 0.62 for ODIAC, representing a substantial 20%–30% improvement over the original scheme. Similarly, for BOXO, R increased from 0.30 to 0.37 with UNAM\_EMI and from 0.22 to 0.35 with ODIAC, accounting for 12.3%–21.7% of the total improvement. ALTZ exhibited an improvement from  $-0.2$  to 0.28 based on UNAM\_EMI and from  $-0.22$  to 0.33 for ODIAC, representing a substantial 44%–49.6% enhancement of the total. These results suggest that employing three specific sites contributes to the coherence of observations at the remaining four sites. RMSE experienced the most significant reduction over BOXO and VALL, whereas it decreased by only less than 5% over ALTZ. This discrepancy can be attributed to the stronger connections between BOXO and VALL with other sites, as illustrated by the IOAMI figure (Figure 1c). Consequently, the corrections around the ALTZ site were relatively minor. Despite this, the noteworthy increase in R for ALTZ and VALL indicates substantial improvements in the distribution of CO<sub>2</sub> emissions surrounding these sites.

Moreover, an assessment of averaging kernel and ER is conducted subsequent to the inversion process (Figure 5). Averaging kernel and the ER is intricately linked with the “H filtered” Q matrix (Equations 5–8). Figures 5a, 5b, 5e, and 5f illustrate the average of the hourly averaging kernel, DOFS, and ER for FF and biogenic sources under our fundamental parameter configuration using the FTIR data set. The spatial pattern of the averaging kernel represents the posterior sensitivity to each grid and varies with different a priori assumptions, as we assume the prior error has a linear relationship with the prior emissions (Equation 11). The total DOFS for the 7-month period is 15,655.3, with an hourly average of 3.05. The hourly DOFS for FF is 1.7, for biogenic sources is 0.8, and the remainder is attributed to the background. The primary sensitivity region and reduction in errors attributed to FF sources is concentrated in urban areas, observed in both UNAM\_EMI and ODIAC. The hourly mean ER over MCMA is 4.23% and 2.93% for UNAM\_EMI and ODIAC, respectively. The reduction in errors related to biogenic sources ranges from 1.9% to 2.13%. As depicted in the second row of Figures 5e and 5f, the magnitude of ER increases with the number of observations at specific time points. When restricting the analysis to times with available observations, the ER intensifies to 7.46% for UNAM\_EMI and 4.69% for ODIAC. Correspondingly, the reduction in biogenic errors is 3.91% and 4.38%. The distribution of ER is further influenced by the number of observations at each site. Time series with a higher volume of data exhibit a more substantial reduction in errors.

A sensitivity analysis serves as a fundamental diagnostic tool, facilitating an understanding of the repercussions stemming from decisions made regarding input parameters on the estimated fluxes (Yadav et al., 2023). The sensitivity test, depicted in Figure 6, encompasses various parameters outlined in Table 1. The sensitivity to these parameters is evaluated through the examination of R and RMSE of the simulated and observed XCO<sub>2</sub> enhancements (as delineated in Figures 4a and 4b), and an additional focus on three state vectors (FF CO<sub>2</sub> flux, biogenic CO<sub>2</sub> flux and background values), and DOFS as shown in Figure 6. It is important here to clarify that this evaluation is a controlled experiment, wherein only one variable is adjusted, whereas the remaining values are held as basic settings (Marked with asterisks in Table 1). This single-variable approach aims to distinctly illustrate

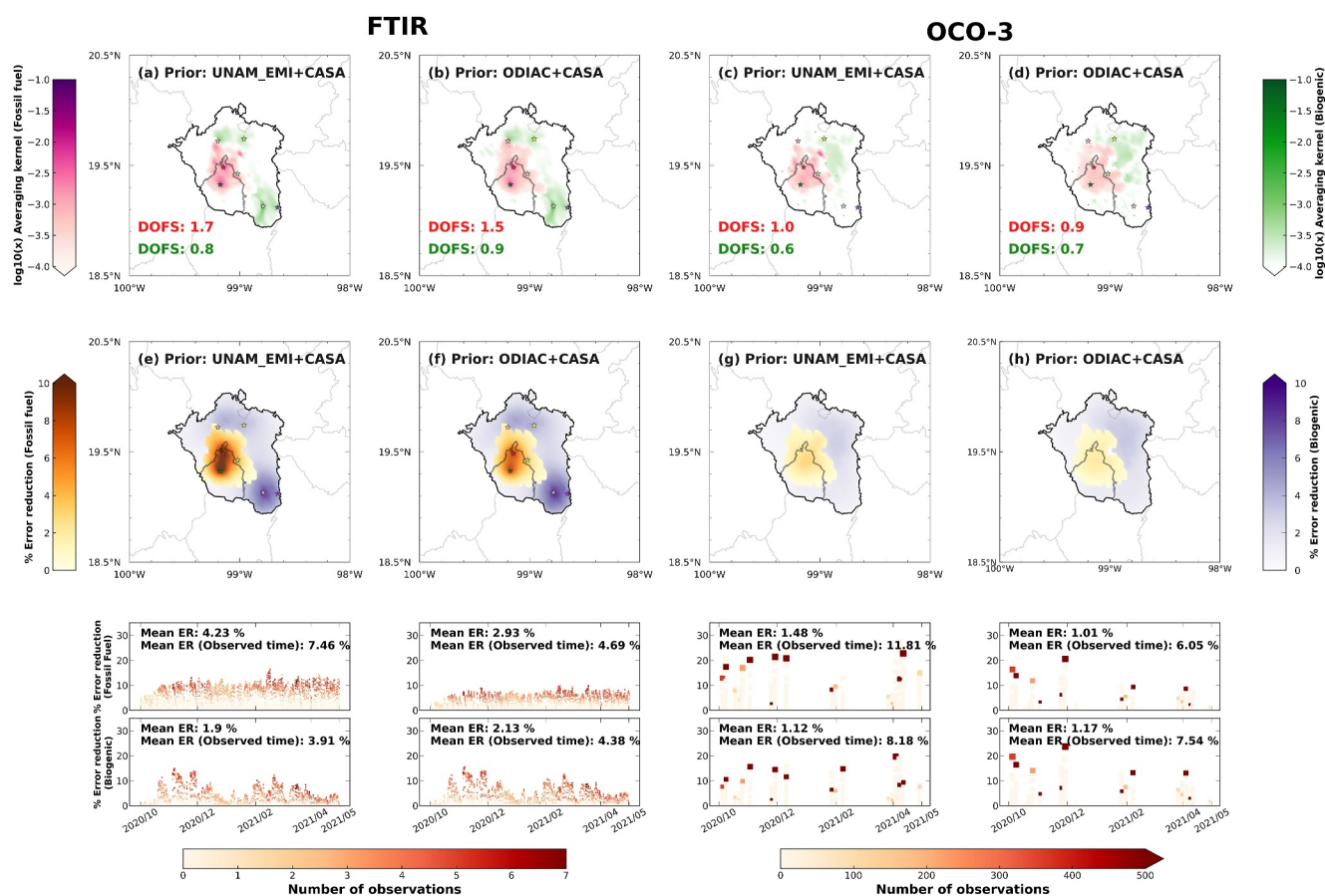


**Figure 5.** Comparison of averaging kernel and error reduction (ER) using Fourier transform infrared and OCO-3 data sets. Panels (a–d) display the average of the hourly averaging kernel, with pink error bars representing fossil fuel (FF) and green error bars representing biogenic sources. DOFS are also indicated in the diagrams. Panels (e–f) illustrate the averaged hourly ER, where red denotes FF and purple indicates biogenic sources. The time series for FF and biogenic sources are shown below, with the colorbar indicating the number of observations used at each time point.

the sensitivity of the results to variations in each selected variable. All units conform to the standards commonly employed in Lagrangian inversion studies (Kunik et al., 2019; Lauvaux et al., 2016; Nevison et al., 2018).

Initially, we analyze the first and second columns of Figure 6 (R and RMSE), representing a comprehensive comparison of the  $\Delta XCO_2$  posterior simulation and observations. Different variations in parameters exhibit consistent patterns for both ODIAC and UNAM\_EMI. It is worth noting that the majority of these curves demonstrate a tendency to stabilize as we systematically test the parameters across a broad range of values. Each parameter, characterized by unique units, undergoes a calculation of maximum-to-minimum values to assess its impact on our results. The parameter with the most substantial influence is  $R_{trans,percent}$ , presenting an R range of 0.26–0.35 and an RMSE of 0.55–0.58 ppm. A larger  $R_{trans,percent}$  aligns the results more closely with the prior values. Subsequently, we evaluate the impact of FF parameters ( $b_{ff}$  and  $l_{s,ff}$ ), revealing an R range of 0.11 and an RMSE range of 0.25–0.29 ppm for  $b_{ff}$ , and an R range of 0.06 and an RMSE range of 0.11–0.16 ppm for  $l_{s,ff}$ . Following this, the parameter  $b_{bio}$  is considered, displaying an R range of 0.03–0.04 and an RMSE range of 0.09–0.1 ppm. It is worth noting that three temporal covariance parameters ( $l_{\tau,ff}$ ,  $l_{\tau,bio}$ ,  $l_{\tau,back}$ ) exhibit minimal influence on the results, as reflected in an R change of 0–0.01 and an RMSE change of 0–0.03 ppm. The DOFS (last column of Figure 6) is sensitive to the temporal covariance parameters for FF and biogenic sources ( $l_{\tau,ff}$ ,  $l_{\tau,bio}$ ) and the prior uncertainty parameters ( $b_{ff}$ ,  $b_{bio}$ ), showing a trend similar to Ohya et al. (2023). The spatial covariance parameters ( $l_{s,ff}$ ,  $l_{s,bio}$ ) cause the DOFS to increase, plateau, and then decrease, following the same trend observed in the synthetic data study by Wu et al. (2018). The parameter  $R_{trans,percent}$  has a different effect, leading to a decrease in DOFS as  $R_{trans,percent}$  increases.

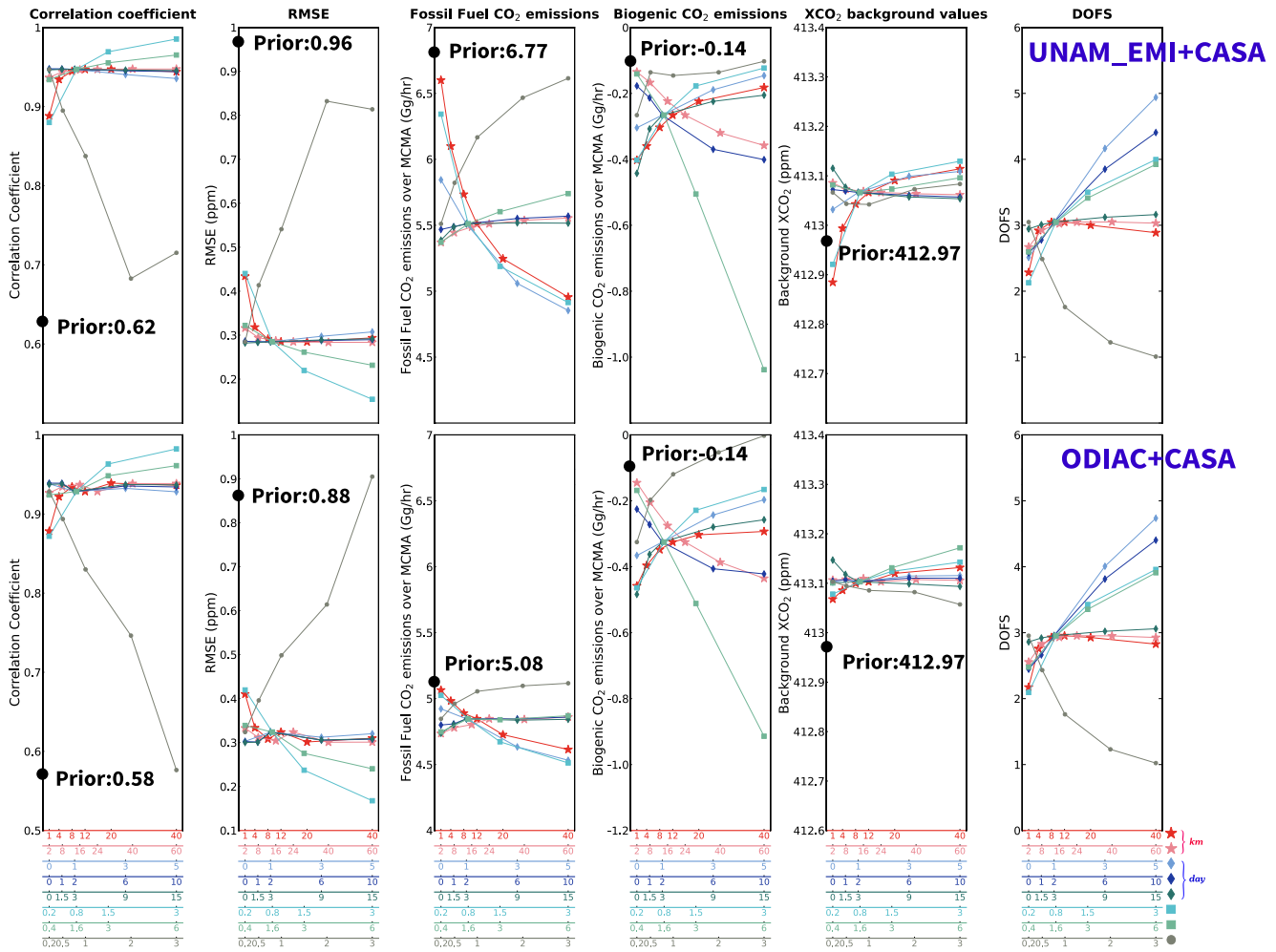


**Figure 6.** Sensitivity analysis of inversion results with UNAM\_EMI (upper panel) and ODIAC priors (lower panel) to various parameters. Each column illustrates the sensitivity test for the following variables: R and root mean square error between simulation and observation, fossil fuel CO<sub>2</sub> emissions, biogenic CO<sub>2</sub> emissions, background values, and DOFS. Parameters, aligned in the same order as Table 1, are presented on the x-axis from top to bottom. The upper triangle points in the figure correspond to the respective prior values for each variable.

Subsequently, we scrutinize the sensitivity of three optimization state vectors to various parameters, with a specific focus on FF and biogenic CO<sub>2</sub> emissions over MCMA, alongside XCO<sub>2</sub> background values. In the context of FF CO<sub>2</sub> emissions over MCMA, the influences of  $l_{s,ff}$ ,  $b_{ff}$ , and  $l_{\tau,ff}$  demonstrate parallel trends: higher values of these variables are associated with lower FF CO<sub>2</sub> emissions. The range of FF CO<sub>2</sub> emissions over MCMA is 1.68 GgCO<sub>2</sub>/hr for UNAM\_EMI and 0.45 GgCO<sub>2</sub>/hr for ODIAC, influenced by  $l_{s,ff}$ . For  $b_{ff}$ , the corresponding change is 1.43 GgCO<sub>2</sub>/hr for UNAM\_EMI and 0.51 GgCO<sub>2</sub>/hr for ODIAC. Regarding  $l_{\tau,ff}$ , the impact is observed as 0.99 GgCO<sub>2</sub>/hr for UNAM\_EMI and 0.39 GgCO<sub>2</sub>/hr for ODIAC. Conversely, parameters originating from biogenic ( $l_{s,bio}$ ,  $b_{bio}$ , and  $l_{\tau,bio}$ ) and transport error ( $R_{trans,percent}$ ) yield opposite effects: increasing these parameters leads to an increase in FF CO<sub>2</sub> emissions, although they remain lower than the prior estimates. Essentially, higher values of these parameters diminish the downward correction power of the data set, making it less substantial. It is worth noting that  $R_{trans,percent}$  emerges as a pivotal parameter influencing the inversion results, exhibiting a change of 1.10 GgCO<sub>2</sub>/hr for UNAM\_EMI and 0.27 GgCO<sub>2</sub>/hr for ODIAC. Regarding biogenic and background parameters, the observed changes are relatively minor, ranging from 0.06 to 0.13 GgCO<sub>2</sub>/hr for ODIAC and 0.10–0.18 GgCO<sub>2</sub>/hr for UNAM\_EMI. In the case of biogenic CO<sub>2</sub> emissions, the most influential parameter is  $b_{bio}$ , contributing to a change in results ranging from 0.75 to 0.90 GgCO<sub>2</sub>/hr. This significance is emphasized by the absence of a clear flattening trend, particularly when opting for higher values of  $b_{bio}$ . Subsequent parameters,  $l_{s,bio}$  and  $l_{\tau,bio}$ , evoke similar responses from UNAM\_EMI and ODIAC, with

changes in biogenic CO<sub>2</sub> emissions ranging from 0.22 to 0.29 for  $l_{s, bio}$  and 0.20 to 0.22 for  $l_{\tau, bio}$  and also impact biogenic CO<sub>2</sub> results (0.23–0.24 GgCO<sub>2</sub>/hr for  $b_{ff}$  and 0.28–0.30 GgCO<sub>2</sub>/hr for  $l_{\tau, back}$ ), whereas  $l_{s, ff}$  (0.09–0.17 GgCO<sub>2</sub>/hr) and  $l_{\tau, ff}$  (0.16–0.17 GgCO<sub>2</sub>/hr) exhibit comparatively lesser effects. Concerning the optimized background values, it is evident that these values do not exert significant influence and quickly stabilize. The total change is particularly concentrated between 413 and 413.1 ppm. The most impactful parameters are  $l_{s, ff}$  and  $b_{ff}$ , contributing changes of 0.24 and 0.21 ppm, with ODIAC exhibiting a change of 0.06 ppm. For the background temporal parameter  $l_{\tau, back}$ , the observed change is only 0.05–0.06 ppm. This phenomenon can be attributed to the relatively modest temporal variations in CAMS, resulting in limited impact from temporal correlation length on the inversion results.

Kunik et al. (2019) systematically examined the effect of covariance parameters through extensive sensitivity studies to assess their impact on inversion results. They discovered that overestimating these parameters results in over-correction of estimates. In Table 1 and Figure 4, we establish the foundational parameters for our inversion study, selected based on the characteristics of the curves. Our primary criteria for parameter selection involve an extensive assessment using curves derived from R and RMSE, providing a comprehensive perspective. It is worth noting that for  $b_{ff}$  and  $b_{bio}$ , it was observed that around 12 and 24 km, the curves tend to stabilize, so these values are chosen as foundational settings. The temporal settings exhibit limited impact on the results, with 1 day chosen for FF, 2 days for biogenic, and 3 days for background values. Upon examination of  $b_{ff}$  and  $b_{bio}$ , it is observed that when  $b_{ff}$  of 0.8 and  $b_{bio}$  of 1.6, the curves tend to plateau. Although larger values of these parameters ( $b_{ff}$  and  $b_{bio}$ ) enhance performance, there is a need to balance this with the  $\chi^2$  value. Larger  $b_{ff}$  and  $b_{bio}$  require matching with very small  $l_{s, ff}$  and  $l_{s, bio}$ , which may not be entirely reasonable. A larger  $R_{trans, percent}$  also brings results closer to the prior estimates, we opt for 0.2 as our basic setting (corresponding to 20% of the simulated  $\Delta XCO_2$  values). In our basic configuration,  $\chi^2$  is 1.03, approximating unity.

### 3.3. Inversion Results for OCO-3

In this section, the inversion is extended to incorporate 19 OCO-3 images collected over the FTIR deployment period. Initial testing focuses on assessing the OCO-3 individual inversion results against OCO-3 observations, as depicted in Figures 4c and 4d, illustrating the model-data mismatch between hourly simulated and observed XCO<sub>2</sub> enhancements. It is worth noting that even when aggregated into spatial resolutions of 5 km, 10 km, 20 km, or 30 km, performances (indicated by hollow triangles to the right) persist in revealing deficiencies. This divergence from the findings in Che et al. (2024b) arises from our previous study's comparison over 7 months, contrasting with the current hourly basis examination. The RMSE of prior results spans from 0.98 to 1.4 ppm, with R values ranging from 0.25 to 0.33 for UNAM\_EMI and from 1.01 to 1.42 ppm with R values ranging from 0.24 to 0.34 for ODIAC. When we use the FTIR posterior results to test coherence with the OCO-3 data set (shown as circles in Figures 4c and 4d), the RMSE ranges from 1.18 ppm at 1 km resolution to 0.68 ppm at 30 km resolution for UNAM\_EMI (improve 15.7% ~ 30.6%), and from 1.16 ppm at 1 km to 0.65 ppm at 30 km for ODIAC (improve 18.3% ~ 35.6%). R increases to 0.31 ~ 0.44 for UNAM\_EMI and 0.34 ~ 0.84 for ODIAC. Upon examining the 1 km posterior results, R increases to 0.61 for UNAM\_EMI and 0.34 for ODIAC, accompanied by a decrease in RMSE to 0.96 ppm for UNAM\_EMI and 1.35 ppm for ODIAC. As we aggregate the posterior into coarser resolutions, coherence with the observations improves. Specifically, for UNAM\_EMI, the R values increase to 0.77, 0.85, 0.93, and 0.95 at resolutions of 5 km, 10 km, 20 km, and 30 km, respectively. Simultaneously, RMSE decreases to 0.61, 0.46, 0.27, and 0.24 ppm for these corresponding resolutions. For ODIAC, R values increase to 0.42, 0.56, 0.77, and 0.84, whereas RMSE decreases to 1.14, 0.87, 0.50, and 0.40 ppm. Additionally, the slopes depicted in this figure demonstrate a consistent increase toward unity with increasing spatial aggregation, rising from 0.44 to 0.88 ppm ppm<sup>-1</sup> for UNAM\_EMI and 0.4–0.85 ppm ppm<sup>-1</sup> for ODIAC.

Moreover, a direct comparison between the corrected emissions during the satellite inversion period and the long-term FTIR inversion results reveals noteworthy findings (Figures 3c, 3d, 3g, and 3h). Specifically, for our OCO-3 inversion results, using UNAM\_EMI and CASA as priors yields a correction of  $-6.44 \pm 22.54\%$  for FF emissions and  $11.1 \pm 100.27\%$  for biogenic emissions. When ODIAC is employed as the prior, the correction for FF is  $0.01 \pm 39.06\%$ , and  $8.62 \pm 194.73\%$  for biogenic emissions. However, the distinctive adjustments in the FTIR inversion results are apparent in FF corrections, demonstrating a reduction of  $-20.52 \pm 16.48\%$  for UNAM\_EMI and  $-6.7 \pm 15.47\%$  for ODIAC (choosing results the same as OCO-3 inversion time). Correspondingly, the uncertainty of differences in biogenic corrections are more pronounced, depicting a substantial decline of



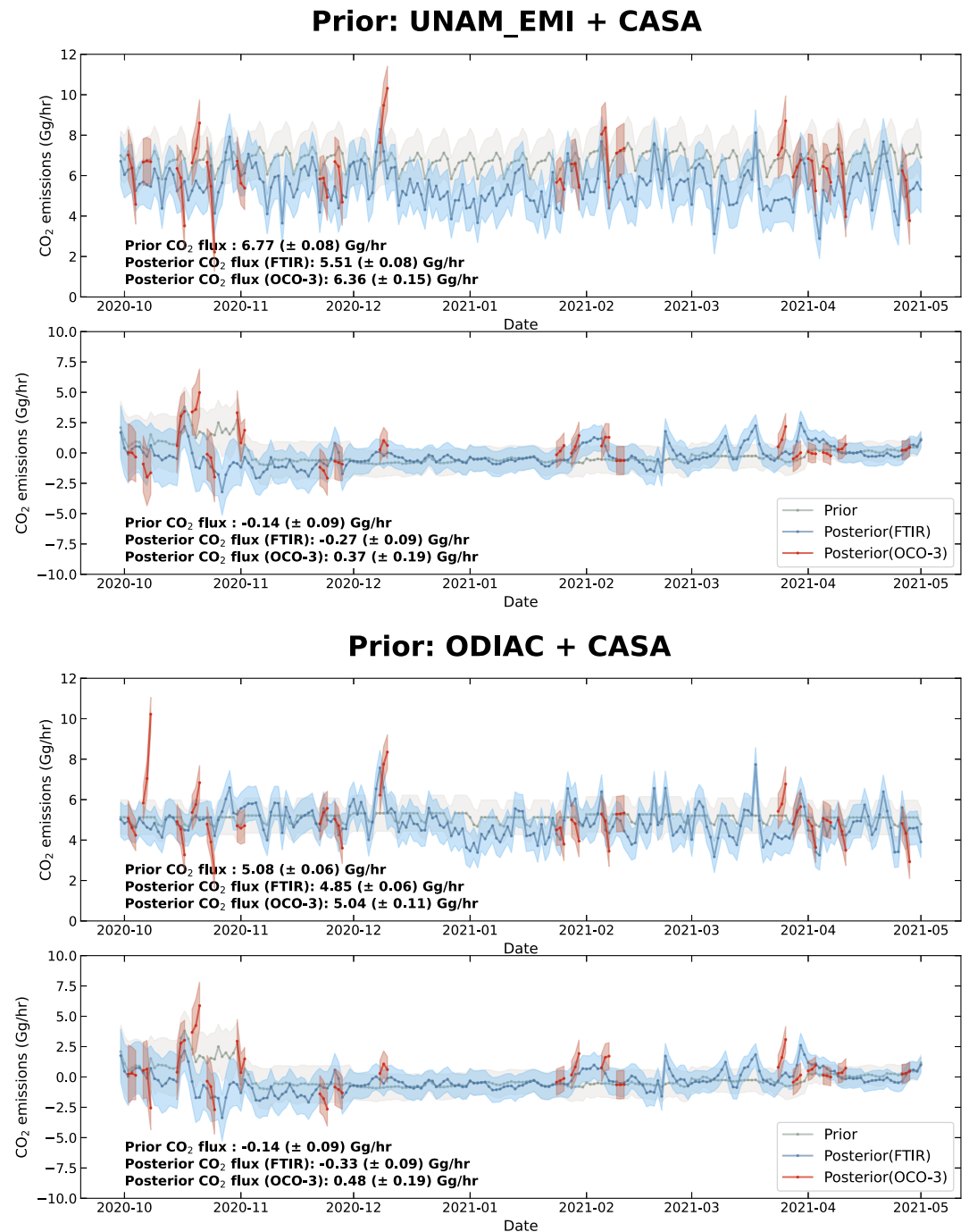


**Figure 7.** Daily biogenic fluxes and fossil fuel emissions (in GgCO<sub>2</sub>/hr) a priori and optimized using OCO-3 and Fourier transform infrared data over the deployment period.

$-32.2 \pm 88.59\%$  for UNAM\_EMI and  $-32.47 \pm 91.63\%$  for ODIAC. The initial conjecture for this substantial disparity arises from the differing sounding times of OCO-3 and FTIR. To address the potential differences arising from sounding times, we specifically selected FTIR data sets with the same sounding times as OCO-3 (only 63 observations out of the total 5,228 observations), presenting the results in Figures 3c, 3d, 3g, 3h, and 7. The correction for FF emissions from FTIR ( $-6.41 \pm 8.59\%$  for UNAM\_EMI and  $-0.93 \pm 7.18\%$  for ODIAC) closely aligns with OCO-3, with only a slightly more negative adjustment to the emissions. However, for the biogenic component, substantial differences persist, indicating adjustments in different directions. Despite these

differences, the correction in this inversion scheme for FTIR remains more consistent compared to the case of inversion using all FTIR observations. The biogenic correction for FTIR remains negative ( $-3.43\%$  to  $-2.82\%$ ), whereas for OCO-3, it is positive ( $8.62\%$ – $11.1\%$ ). Even when using the same time points, discrepancies persist in the results. The primary reason, as seen in the averaging kernel comparison plot, is attributed to the different sampling locations of the two instruments, as depicted in Figures S2, S3c, and S3d in Supporting Information S1. Additionally, XCO<sub>2</sub> discrepancies in observations between OCO-3 and FTIR, or measurement errors associated with OCO-3, contribute to these differences. It is challenging to determine which observation type produces more robust results without connecting additional FF or biogenic tracer gases.

The subsequent examination focuses on the temporal results between the two inversion outcomes. Figure 7 illustrates the daily CO<sub>2</sub> flux from both FTIR and OCO-3 inversion results. A comprehensive assessment of the overall CO<sub>2</sub> flux over the 7-month period reveals a reduction in the FF component in both inversion results. The total mean prior CO<sub>2</sub> flux for the entire inversion time series is  $6.77 (\pm 0.08)$  GgCO<sub>2</sub>/hr, with the value in parentheses representing the root square sum of prior uncertainty for the whole inversion period, not one standard deviation. Specifically, the mean FF CO<sub>2</sub> with FTIR constraints is  $5.51 (\pm 0.08)$  GgCO<sub>2</sub>/hr, compared to  $6.36 (\pm 0.15)$  GgCO<sub>2</sub>/hr for OCO-3. Both FTIR and OCO-3 show a tendency to negatively adjust the initially over-estimated UNAM\_EMI emissions. Concerning the biogenic part, the prior estimates indicate  $-0.14 (\pm 0.09)$  GgCO<sub>2</sub>/hr, whereas the posterior estimates based on FTIR and OCO-3 are  $-0.27 (\pm 0.09)$  GgCO<sub>2</sub>/hr and  $0.37 (\pm 0.19)$  GgCO<sub>2</sub>/hr, respectively. The sign of biogenic flux correction differs, and this discrepancy is not attributed to the sounding time of the two instruments as proved in the last paragraph. When adopting ODIAC and CASA as priors, the prior CO<sub>2</sub> fossil flux is determined to be  $5.08 (\pm 0.06)$  GgCO<sub>2</sub>/hr. Subsequently, the CO<sub>2</sub> FF flux in the posterior results is observed to be  $4.85 (\pm 0.06)$  GgCO<sub>2</sub>/hr and  $5.04 (\pm 0.11)$  GgCO<sub>2</sub>/hr based on FTIR and OCO-3, respectively. Despite the alignment in the correction direction, the correction from FTIR for the FF component is more pronounced. Regarding the biogenic component, the adjustments for FTIR ( $-0.33 (\pm 0.09)$  GgCO<sub>2</sub>/hr) and OCO-3 ( $0.48 (\pm 0.19)$  GgCO<sub>2</sub>/hr) exhibit dissimilar trends. The discrepancies observed in Figure S10 in Supporting Information S1 prompt us to explore the reasons behind the divergent results between FTIR and OCO-3 on certain days. The study maintains uniformity in error structure, prior estimates, and parameters. The primary distinction lies in the inherent differences between OCO-3 and FTIR, along with the measurement error of OCO-3. We discard the possibility of FTIR measurement errors, given its stable and consistent nature throughout the time series. Figure S5 in Supporting Information S1 illustrates the XCO<sub>2</sub> measurement errors of OCO-3 and the disparity between FTIR and OCO-3. It is worth noting that on 21 October 2020 and 26 March 2021, substantial differences between FTIR and OCO-3, reaching 5.09 and 3.24 ppm over the VALL and BOXO sites, respectively, lead to corrections in opposing directions for both data sets.

#### 4. Discussion and Conclusions

This study assessed CO<sub>2</sub> emissions over the Metropolitan Area of Mexico City (MCMA) by utilizing a dense ground-based FTIR network and space-based OCO-3 SAMs observations, with a focus on finer spatial scales for evaluating FF and biogenic emissions of CO<sub>2</sub> over October 2020 to May 2021. Three prior inventories, including two for FF emissions (UNAM\_EMI, ODIAC) and one accounting for biogenic activities (CASA), were optimized in conjunction with an computational analytical Bayesian inversion technique to robustly update prior estimates at 1-km and 1-hr resolution. Leveraging the X-STILT, driven by WRF at a 1-km resolution, we connected atmospheric observations to surface fluxes and background conditions. According to the column footprints from X-STILT, our FTIR observations are influenced by the emissions throughout central Mexico. To find a balance between accuracy and computational efficiency, we conducted a sensitivity analysis to select the optimal inversion area, comparing approaches focusing solely on MCMA versus the entire central Mexico. Results indicated minor differences in the corrections applied within MCMA between the two approaches, particularly for UNAM\_EMI (1.95% correction difference) and ODIAC (0.08% correction difference), with negligible differences for biogenic emissions. The UNAM\_EMI is more sensitive to the region selection test than ODIAC is due to its inclusion of a power station located outside the MCMA. Consequently, we have designated the MCMA as the focal area for our inversion analysis.

In addition to selecting a reasonable region for inversion, it is imperative to choose appropriate parameters for the inversion system, as delineated in Table 1. An extensive control experiment was conducted to evaluate the impact of various uncertain parameters on the inversion results. Through a comprehensive assessment of both posterior outcomes and observational data, we identified transport error as a critical factor. This error significantly

undermines the corrective capacity of our inversion system; a higher transport error leads to minimal adjustments, rendering posterior results nearly identical to the prior estimations. This underscores the necessity of acquiring more accurate meteorological data and a robust transport model. Among the parameters evaluated, prior uncertainty and spatial covariance parameters emerged as notably influential, whereas temporal parameters had a lesser impact on the posterior outcomes. This variation in influence is likely attributed to gaps in FTIR measurement observations. Regarding emissions corrections, FF CO<sub>2</sub> emissions are significantly affected by prior uncertainty, spatial, and temporal covariance parameters related to FF sources. Similarly, biogenic CO<sub>2</sub> emissions predominantly impact biogenic parameters, with posterior background values showing lesser sensitivity to these fluctuations. An increased error covariance for FF (or biogenic) part typically results in a more substantial negative correction for FF (or biogenic) emissions. This is due to a larger covariance that propagates the observed negative correction to nearby grids, leading to a more pronounced decrease. An increase in biogenic covariance results in positive FF corrections due to the opposite effect: a larger negative correction for biogenic emissions under the same overall observational correction, necessitating a compensatory adjustment in the opposite direction for other parameters.

We selected the most reasonable parameters, those corresponding to the curve's plateau, as our basic configuration. This setup allowed us to achieve a  $\chi^2$  value of 1 and enhanced coherence with the observational data. Based on this configuration, we found a 1.26 GgCO<sub>2</sub>/hr (18.73%) overestimation in UNAM\_EMI and a 0.23 GgCO<sub>2</sub>/hr (5.88%) overestimation in ODIAC, the most correction region is within the urban area. The correction for the biogenic part remains relatively small in the FTIR inversion (−0.18 ~ −0.12 GgCO<sub>2</sub>/hr), possibly due to the largest FF signals (3–4 times greater than the biogenic signal) in our modeling domain. The posterior analysis reveals a reduction in the FF component, from an initial range of 5.08–6.77 Gg CO<sub>2</sub>/hr, narrowing down to between 5.04 and 5.51 Gg CO<sub>2</sub>/hr. There was also a decrease in the biogenic emissions, with values shifting from −0.14 Gg CO<sub>2</sub>/hr to a range of −0.27 to −0.33 Gg CO<sub>2</sub>/hr over the span of 7 months. The correction for the FF part is significant and tends to bring posterior results from the UNAM\_EMI and ODIAC prior emission data closer. However, discrepancies still exist between the posterior results and the priors from the two inventories. The main reason for this is the different structures of the priors, which also affect the averaging kernel structure. The ER for hourly FF emissions ranges between 3% and 4%, and for biogenic emissions, it is 2%. The extent of this ER is aligned with the temporal focus of our corrections, such as annual or monthly adjustments (Lauvaux et al., 2020). Given our emphasis on hourly corrections, these values are appropriately modest. When compared the simulated  $\Delta XCO_2$  from prior and posterior emissions with observations, it revealed that posterior results are more robust, greatly improving the coherence of simulation and observations. Employing subsets of our FTIR data sets has also proven to be beneficial for the remaining data sets.

The inversion analysis was expanded through the incorporation of OCO-3 SAM observations. The refined estimates indicate FF CO<sub>2</sub> emissions ranging from 5.04 to 6.36 GgCO<sub>2</sub>/hr and biogenic emissions between 0.37 and 0.48 GgCO<sub>2</sub>/hr. The ER for OCO-3 is only significant during the overpass time, reaching 8%–11% for FF and 6.1%–7.5% for biogenic sources. The averaging kernel demonstrates the observational constraint sensitivity on the surrounding grid. Both FTIR and OCO-3 are sensitive to the urban region of MCMA; however, the biogenic sensitivity differs. FTIR is sensitive to both the north and south, whereas OCO-3 is only sensitive to the northeast part of MCMA, which corresponds to the ER. The DOFS for OCO-3 is lower than FTIR on an hourly basis, and the DOFS for FF is greater than for biogenic sources in both the FTIR and OCO-3 data sets. A comparison of the posterior simulated results with OCO-3 observations revealed that coherence did not significantly improve at the original resolution. However, upon aggregating the data to a coarser resolution (from 1 to 30 km), a substantial enhancement in alignment with observations was observed, suggesting that OCO-3 observations could be used to constrain urban emissions by mitigating random observational errors. In addition, comparing the FTIR posterior results with OCO-3 observations provides an independent evaluation, demonstrating that the FTIR posterior results are enhancing the prior inventories. Differences between the OCO-3 inversion results and those from FTIR inversions were noted and the impact of sparse temporal density in OCO-3 data was evident: using FTIR data in OCO-3 overpass time resulted in similar FF corrections for both OCO-3 and FTIR (−0.47 to 0.44 GgCO<sub>2</sub>/hr for UNAM\_EMI and −0.05 to −0.01 GgCO<sub>2</sub>/hr for ODIAC). However, the two data sets showed divergent corrections for biogenic emissions, with OCO-3 adjusting upward (0.21–0.31 GgCO<sub>2</sub>/hr) and FTIR adjusting downward (−0.3 to −0.28 GgCO<sub>2</sub>/hr), highlighting the complexities in accurately constraining the biogenic component in this inversion framework. The limited rural observations by OCO-3, differences in sampling locations, and observed XCO<sub>2</sub> disparities between OCO-3 and FTIR contributed to discrepancies in the inversion

outcomes, including divergent correction directions. In prospective, the incorporation of supplementary constraints derived from tracer gasses such as NO<sub>x</sub>, CO, or radiocarbon, or a direct juxtaposition of posterior flux outcomes against eddy flux towers, will significantly enhance the evaluation of methodological robustness. This is particularly pertinent in the context of refining the optimization of the FF component once the accurate calculation of the biogenic portion has been established.

### Data Availability Statement

The FTIR observation data are accessible on (Ramonet et al., 2024). The OCO-3 Level 2 bias-corrected XCO<sub>2</sub> data (version 10.4r) are available for download from (OCO-2/OCO-3 Science Team et al., 2022). The ERA5 data are accessible at (Hersbach et al., 2022). CAMS global inversion-optimized greenhouse gas concentrations are accessible at the Copernicus Climate Change Service (C3S) Climate Data Store (Chevallier, 2013; Chevallier et al., 2019, 2023). The ODIAC emission inventory is documented in Oda and Maksyutov (2015). The inversion results for FTIR and OCO-3 could be assess from Che et al. (2024a).

### References

Ahn, D., Goldberg, D., Coombes, T., Kleiman, G., & Anenberg, S. (2023). CO<sub>2</sub> emissions from C40 cities: Citywide emission inventories and comparisons with global gridded emission datasets. *Environmental Research Letters*, 18(3), 034032. <https://doi.org/10.1088/1748-9326/acbb91>

Alberti, C., Hase, F., Frey, M., Dubravica, D., Blumenstock, T., Dehn, A., et al. (2022). Improved calibration procedures for the EM27/SUN spectrometers of the Collaborative Carbon Column Observing Network (COCCON). *Atmospheric Measurement Techniques*, 15(8), 2433–2463. <https://doi.org/10.5194/amt-15-2433-2022>

Bell, E., O'Dell, C. W., Taylor, T. E., Merrelli, A., Nelson, R. R., Kiel, M., et al. (2023). Exploring bias in the OCO-3 snapshot area mapping mode via geometry, surface, and aerosol effects. *Atmospheric Measurement Techniques*, 16(1), 109–133. <https://doi.org/10.5194/amt-16-109-2023>

Cai, Z., Che, K., Liu, Y., Yang, D., Liu, C., & Yue, X. (2021). Decreased anthropogenic CO<sub>2</sub> emissions during the COVID-19 pandemic estimated from FTS and MAX-DOAS measurements at urban Beijing. *Remote Sensing*, 13(3), 517. <https://doi.org/10.3390/rs13030517>

Che, K., Cai, Z., Liu, Y., Wu, L., Yang, D., Chen, Y., et al. (2022). Lagrangian inversion of anthropogenic CO<sub>2</sub> emissions from Beijing using differential column measurements. *Environmental Research Letters*, 17(7), 075001. <https://doi.org/10.1088/1748-9326/ac7477>

Che, K., Lauvaux, T., Taquet, N., Stremme, W., Xu, Y., Alberti, C., et al. (2024a). CO<sub>2</sub> emissions estimate from Mexico City using ground- and space-based remote sensing [Dataset]. <https://doi.org/10.5281/zenodo.13147330>

Che, K., Lauvaux, T., Taquet, N., Stremme, W., Xu, Y., Alberti, C., et al. (2024b). Urban XCO<sub>2</sub> gradients from a dense network of solar absorption spectrometers and OCO-3 over Mexico City. *Journal of Geophysical Research: Atmospheres*, 129(9), e2023JD040063. <https://doi.org/10.1029/2023JD040063>

Chen, G., Shan, Y., Hu, Y., Tong, K., Wiedmann, T., Ramaswami, A., et al. (2019). Review on city-level carbon accounting. *Environmental Science & Technology*, 53(10), 5545–5558. <https://doi.org/10.1021/acs.est.8b07071>

Chen, H. W., Zhang, F., Lauvaux, T., Scholze, M., Davis, K. J., & Alley, R. B. (2023). Regional CO<sub>2</sub> inversion through ensemble-based simultaneous state and parameter estimation: Trace framework and controlled experiments. *Journal of Advances in Modeling Earth Systems*, 15(3), e2022MS003208. <https://doi.org/10.1029/2022ms003208>

Chen, J., Viatte, C., Hedelius, J. K., Jones, T., Franklin, J. E., Parker, H., et al. (2016). Differential column measurements using compact solar-tracking spectrometers. *Atmospheric Chemistry and Physics*, 16(13), 8479–8498. <https://doi.org/10.5194/acp-16-8479-2016>

Chevallier, F. (2013). On the parallelization of atmospheric inversions of CO<sub>2</sub> surface fluxes within a variational framework. *Geoscientific Model Development*, 6(3), 783–790. <https://doi.org/10.5194/gmd-6-783-2013>

Chevallier, F., Lloret, Z., Cozic, A., Takache, S., & Remaud, M. (2023). Toward high-resolution global atmospheric inverse modeling using graphics accelerators. *Geophysical Research Letters*, 50(5), e2022GL102135. <https://doi.org/10.1029/2022GL102135>

Chevallier, F., Remaud, M., O'Dell, C. W., Baker, D., Peylin, P., & Cozic, A. (2019). Objective evaluation of surface- and satellite-driven carbon dioxide atmospheric inversions. *Atmospheric Chemistry and Physics*, 19(22), 14233–14251. <https://doi.org/10.5194/acp-19-14233-2019>

Chevallier, F., Wang, T., Ciais, P., Maignan, F., Bocquet, M., Altaf Arain, M., et al. (2012). What eddy-covariance measurements tell us about prior land flux errors in CO<sub>2</sub>-flux inversion schemes. *Global Biogeochemical Cycles*, 26(1). <https://doi.org/10.1029/2010GB003974>

Cusworth, D. H., Thorpe, A. K., Miller, C. E., Ayasse, A. K., Jiorle, R., Duren, R. M., et al. (2023). Two years of satellite-based carbon dioxide emission quantification at the world's largest coal-fired power plants. *Atmospheric Chemistry and Physics*, 23(22), 14577–14591. <https://doi.org/10.5194/acp-23-14577-2023>

Desroziers, G., Arbogast, E., & Berre, L. (2016). Improving spatial localization in 4D-EnVar. *Quarterly Journal of the Royal Meteorological Society*, 142(701), 3171–3185. <https://doi.org/10.1002/qj.2898>

Dietrich, F., Chen, J., Voggenreiter, B., Aigner, P., Nachtigall, N., & Reger, B. (2021). MUCNet: Munich urban carbon column network. *Atmospheric Measurement Techniques*, 14(2), 1111–1126. <https://doi.org/10.5194/amt-14-1111-2021>

Dorrell, D., Connor, G., Henderson, J., Lindley, T., Dohrenwend, A., Ibáñez, J., et al. (2024). *Human settlements*. Introduction to Human Geography.

Eldering, A., Taylor, T. E., O'Dell, C. W., & Pavlick, R. (2019). The OCO-3 mission: Measurement objectives and expected performance based on 1 year of simulated data. *Atmospheric Measurement Techniques*, 12(4), 2341–2370. <https://doi.org/10.5194/amt-12-2341-2019>

Gately, C. K., & Hutyrá, L. R. (2017). Large uncertainties in urban-scale carbon emissions. *Journal of Geophysical Research: Atmospheres*, 122(20), 11–242. <https://doi.org/10.1002/2017JD027359>

Gately, C. K., Hutyrá, L. R., & Sue Wing, I. (2015). Cities, traffic, and CO<sub>2</sub>: A multidecadal assessment of trends, drivers, and scaling relationships. *Proceedings of the National Academy of Sciences*, 112(16), 4999–5004. <https://doi.org/10.1073/pnas.1421723112>

Gómez-Ortiz, C., Monteil, G., Basu, S., & Scholze, M. (2023). Can Δ<sup>14</sup>C<sub>2</sub> observations help atmospheric inversions constrain the fossil CO<sub>2</sub> emission budget of Europe? *EGU sphere*, 2023, 1–36. <https://doi.org/10.5194/egusphere-2023-2215>

### Acknowledgments

The measurement campaign was funded by the CONACYT-ANR project 290589 “Mexico City's Regional Carbon Impacts” (ANR-17-CE04-0013-01). Alejandro Bezanilla and Omar López are thanked for their support in installing and operating the instruments during the campaign.



- Guo, B., Xie, T., Zhang, W., Wu, H., Zhang, D., Zhu, X., et al. (2023). Rasterizing CO<sub>2</sub> emissions and characterizing their trends via an enhanced population-light index at multiple scales in China during 2013–2019. *Science of the Total Environment*, 905, 167309. <https://doi.org/10.1016/j.scitotenv.2023.167309>
- Gurney, K. R., Liang, J., O'keeffe, D., Patarasuk, R., Hutchins, M., Huang, J., et al. (2019). Comparison of global downscaled versus bottom-up fossil fuel CO<sub>2</sub> emissions at the urban scale in four US urban areas. *Journal of Geophysical Research: Atmospheres*, 124(5), 2823–2840. <https://doi.org/10.1029/2018JD028859>
- Gurney, K. R., Romero-Lankao, P., Seto, K. C., Hutrya, L. R., Duren, R., Kennedy, C., et al. (2015). Climate change: Track urban emissions on a human scale. *Nature*, 525(7568), 179–181. <https://doi.org/10.1038/525179a>
- Hakkariainen, J., Ialongo, I., Oda, T., Szelag, M. E., O'Dell, C. W., Eldering, A., & Crisp, D. (2023). Building a bridge: Characterizing major anthropogenic point sources in the South African Highveld region using OCO-3 carbon dioxide snapshot area maps and Sentinel-5P/TROPOMI nitrogen dioxide columns. *Environmental Research Letters*, 18(3), 035003. <https://doi.org/10.1088/1748-9326/acb837>
- Hase, F., Frey, M., Blumenstock, T., Groß, J., Kiel, M., Kohlhepp, R., et al. (2015). Application of portable FTIR spectrometers for detecting greenhouse gas emissions of the major city Berlin. *Atmospheric Measurement Techniques*, 8(7), 3059–3068. <https://doi.org/10.5194/amt-8-3059-2015>
- Hersbach, H., Bell, B., Berrisford, P., Biavati, G., Horányi, A., Muñoz Sabater, J., et al. (2022). ERA5 hourly data on single levels from 1940 to present [Dataset]. *Copernicus Climate Change Service (C3S) Climate Data Store (CDS)*. <https://doi.org/10.24381/cds.adbb2d47>
- Hong, S., man Hui, E. C., & Lin, Y. (2022). Relationship between urban spatial structure and carbon emissions: A literature review. *Ecological Indicators*, 144, 109456. <https://doi.org/10.1016/j.ecolind.2022.109456>
- Humpage, N., Boesch, H., Okello, W., Chen, J., Dietrich, F., Lunt, M. F., et al. (2023). Greenhouse gas column observations from a portable spectrometer in Uganda. *Atmospheric Measurement Techniques Discussions*, 2023, 1–34. <https://doi.org/10.5194/amt-2023-234>
- Huo, D., Huang, X., Dou, X., Ciais, P., Li, Y., Deng, Z., et al. (2022). Carbon monitor cities near-real-time daily estimates of CO<sub>2</sub> emissions from 1500 cities worldwide. *Scientific Data*, 9(1), 533. <https://doi.org/10.1038/s41597-022-01657-z>
- Ionov, D. V., Makarova, M. V., Hase, F., Foka, S. C., Kostov, V. S., Alberti, C., et al. (2021). The CO<sub>2</sub> integral emission by the megacity of St Petersburg as quantified from ground-based FTIR measurements combined with dispersion modelling. *Atmospheric Chemistry and Physics*, 21(14), 10939–10963. <https://doi.org/10.5194/acp-21-10939-2021>
- Jones, T. S., Franklin, J. E., Chen, J., Dietrich, F., Hajny, K. D., Paetzold, J. C., et al. (2021). Assessing urban methane emissions using column-observing portable Fourier transform infrared (FTIR) spectrometers and a novel Bayesian inversion framework. *Atmospheric Chemistry and Physics*, 21(17), 13131–13147. <https://doi.org/10.5194/acp-21-13131-2021>
- Kaminski, T., Rayner, P. J., Heimann, M., & Enting, I. G. (2001). On aggregation errors in atmospheric transport inversions. *Journal of Geophysical Research*, 106(D5), 4703–4715. <https://doi.org/10.1029/2000JD900581>
- Kiel, M., Eldering, A., Roten, D. D., Lin, J. C., Feng, S., Lei, R., et al. (2021). Urban-focused satellite CO<sub>2</sub> observations from the Orbiting Carbon Observatory-3: A first look at the Los Angeles megacity. *Remote Sensing of Environment*, 258, 112314. <https://doi.org/10.1525/elementa.137>
- Kunik, L., Mallia, D. V., Gurney, K. R., Mendoza, D. L., Oda, T., & Lin, J. C. (2019). Bayesian inverse estimation of urban CO<sub>2</sub> emissions: Results from a synthetic data simulation over Salt Lake City, UT. *Elementa: Science of the Anthropocene*, 7, 36. <https://doi.org/10.1525/elementa.375>
- Lauvaux, T., & Davis, K. (2014). Planetary boundary layer errors in mesoscale inversions of column-integrated CO<sub>2</sub> measurements. *Journal of Geophysical Research: Atmospheres*, 119(2), 490–508. <https://doi.org/10.1002/2013JD020175>
- Lauvaux, T., Gurney, K. R., Miles, N. L., Davis, K. J., Richardson, S. J., Deng, A., et al. (2020). Policy-relevant assessment of urban CO<sub>2</sub> emissions. *Environmental Science & Technology*, 54(16), 10237–10245. <https://doi.org/10.1021/acs.est.0c00343>
- Lauvaux, T., Miles, N. L., Deng, A., Richardson, S. J., Cambaliza, M. O., Davis, K. J., et al. (2016). High-resolution atmospheric inversion of urban CO<sub>2</sub> emissions during the dormant season of the Indianapolis Flux Experiment (INFLUX). *Journal of Geophysical Research: Atmospheres*, 121(10), 5213–5236. <https://doi.org/10.1002/2015JD024473>
- Li, X., Cohen, J. B., Qin, K., Geng, H., Wu, X., Wu, L., et al. (2023). Remotely sensed and surface measurement-derived mass-conserving inversion of daily NO<sub>x</sub> emissions and inferred combustion technologies in energy-rich northern China. *Atmospheric Chemistry and Physics*, 23(14), 8001–8019. <https://doi.org/10.5194/acp-23-8001-2023>
- Lin, X., Van Der A, R., De Laat, J., Eskes, H., Chevallier, F., Ciais, P., et al. (2023). Monitoring and quantifying CO<sub>2</sub> emissions of isolated power plants from space. *Atmospheric Chemistry and Physics*, 23(11), 6599–6611. <https://doi.org/10.5194/acp-23-6599-2023>
- Lu, X., Jacob, D., Zhang, Y., Maasakkers, J., Sulprizio, M., Shen, L., et al. (2020). Global methane budget and trend, 2010–2017: Complementarity of inverse analyses using in situ (globalviewplus CH<sub>4</sub> obspack) and satellite (gosat) observations. *Atmospheric Chemistry and Physics*. <https://doi.org/10.5194/acp-2020-775>
- Luther, A., Kleinschek, R., Scheidweiler, L., Defratyka, S., Stanisavljevic, M., Forstmaier, A., et al. (2019). Quantifying CH<sub>4</sub> emissions from hard coal mines using mobile sun-viewing Fourier transform spectrometry. *Atmospheric Measurement Techniques*, 12(10), 5217–5230. <https://doi.org/10.5194/amt-12-5217-2019>
- Nalini, K., Lauvaux, T., Abdallah, C., Lian, J., Ciais, P., Utard, H., et al. (2022). High-resolution Lagrangian inverse modeling of CO<sub>2</sub> emissions over the Paris region during the first 2020 lockdown period. *Journal of Geophysical Research: Atmospheres*, 127(14), e2021JD036032. <https://doi.org/10.1029/2021JD036032>
- Nevison, C., Andrews, A., Thoning, K., Dlugokencky, E., Sweeney, C., Miller, S., et al. (2018). Nitrous oxide emissions estimated with the carbontracker-lagrange north American regional inversion framework. *Global Biogeochemical Cycles*, 32(3), 463–485. <https://doi.org/10.1002/2017gb005759>
- Newman, S., Xu, X., Gurney, K. R., Hsu, Y. K., Li, K. F., Jiang, X., et al. (2016). Toward consistency between trends in bottom-up CO<sub>2</sub> emissions and top-down atmospheric measurements in the Los Angeles megacity. *Atmospheric Chemistry and Physics*, 16(6), 3843–3863. <https://doi.org/10.5194/acp-16-3843-2016>
- OCO-2/OCO-3 Science Team, Chatterjee, A., & Payne, V. (2022). OCO-3 Level 2 bias-corrected XCO<sub>2</sub> and other select fields from the full-physics retrieval aggregated as daily files. Retrospective processing v10.4r [dataset]. Goddard Earth Sciences Data and Information Services Center (GES DISC). <https://doi.org/10.5067/970BCC4DHH24>
- Oda, T., Bun, R., Kinakh, V., Topylko, P., Halushchak, M., Marland, G., et al. (2019). Errors and uncertainties in a gridded carbon dioxide emissions inventory. *Mitigation and Adaptation Strategies for Global Change*, 24(6), 1007–1050. <https://doi.org/10.1007/s11027-019-09877-2>
- Oda, T., & Maksyutov, S. (2015). ODIAC Fossil Fuel CO<sub>2</sub> Emissions Dataset (ODIAC2020) [Dataset]. *Center for Global Environmental Research, National Institute for Environmental Studies*. <https://doi.org/10.17595/20170411.001>
- Oda, T., Maksyutov, S., & Andres, R. J. (2018). The Open-source Data Inventory for Anthropogenic CO<sub>2</sub>, version 2016 (ODIAC2016): A global monthly fossil fuel CO<sub>2</sub> gridded emissions data product for tracer transport simulations and surface flux inversions. *Earth System Science Data*, 10(1), 87–107. <https://doi.org/10.5194/essd-10-87-2018>

- Ohyama, H., Frey, M. M., Morino, I., Shiomi, K., Nishihashi, M., Miyauchi, T., et al. (2023). Anthropogenic CO<sub>2</sub> emission estimates in the Tokyo metropolitan area from ground-based CO<sub>2</sub> column observations. *Atmospheric Chemistry and Physics*, 23(23), 15097–15119. <https://doi.org/10.5194/acp-23-15097-2023>
- Pisso, I., Patra, P., Takigawa, M., Machida, T., Matsueda, H., & Sawa, Y. (2019). Assessing Lagrangian inverse modelling of urban anthropogenic CO<sub>2</sub> fluxes using in situ aircraft and ground-based measurements in the Tokyo area. *Carbon Balance and Management*, 14, 1–23. <https://doi.org/10.1186/s13021-019-0118-8>
- Qin, K., Lu, L., Liu, J., He, Q., Shi, J., Deng, W., et al. (2023). Model-free daily inversion of NO<sub>x</sub> emissions using TROPOMI (MCMFE-NO<sub>x</sub>) and its uncertainty: Declining regulated emissions and growth of new sources. *Remote Sensing of Environment*, 295, 113720. <https://doi.org/10.1016/j.rse.2023.113720>
- Ramonet, M., Grutter, M., Taquet, N., Lopez, M., & Stremme, W. (2024). CO<sub>2</sub> total columns in Mexico-City [dataset]. <https://doi.org/10.57932/4c264750-4eb4-4cf8-9432-1c79048116d3>
- Ribmann, M., Chen, J., Osterman, G., Zhao, X., Dietrich, F., Makowski, M., et al. (2022). Comparison of OCO-2 target observations to MUCNet—is it possible to capture urban XCO<sub>2</sub> gradients from space? *Atmospheric Measurement Techniques*, 15(22), 6605–6623. <https://doi.org/10.5194/amt-15-6605-2022>
- Roten, D., Lin, J. C., Das, S., & Kort, E. A. (2023). Constraining sector-specific CO<sub>2</sub> fluxes using space-based XCO<sub>2</sub> observations over the Los Angeles basin. *Geophysical Research Letters*, 50(21), e2023GL104376. <https://doi.org/10.1029/2023GL104376>
- Roten, D., Lin, J. C., Kunik, L., Mallia, D., Wu, D., Oda, T., & Kort, E. A. (2022). The information content of dense carbon dioxide measurements from space: A high-resolution inversion approach with synthetic data from the OCO-3 instrument. *Atmospheric Chemistry and Physics Discussions*, 1–43. <https://doi.org/10.5194/acp-2022-315>
- Sargent, M., Barrera, Y., Nehrkorn, T., Hutyra, L. R., Gately, C. K., Jones, T., et al. (2018). Anthropogenic and biogenic CO<sub>2</sub> fluxes in the Boston urban region. *Proceedings of the National Academy of Sciences of the United States of America*, 115(29), 7491–7496. <https://doi.org/10.1073/pnas.1803715115>
- Shan, C., Wang, W., Liu, C., Sun, Y., Hu, Q., Xu, X., et al. (2019). Regional CO emission estimated from ground-based remote sensing at Hefei site, China. *Atmospheric Research*, 222, 25–35. <https://doi.org/10.1016/j.atmosres.2019.02.005>
- Shekhar, A., Chen, J., Paetzold, J. C., Dietrich, F., Zhao, X., Bhattacharjee, S., et al. (2020). Anthropogenic CO<sub>2</sub> emissions assessment of Nile Delta using XCO<sub>2</sub> and SIF data from OCO-2 satellite. *Environmental Research Letters*, 15(9), 095010. <https://doi.org/10.1088/1748-9326/ab9cfe>
- Taquet, N., Stremme, W., Gonzalez del Castillo, M. E., Almanza, V., Bezanilla, A., Laurent, O., et al. (2024). CO<sub>2</sub> and CO temporal variability over Mexico City from ground-based total column and surface measurements. *Atmospheric Chemistry and Physics*, 24(20), 11823–11824. <https://doi.org/10.5194/acp-24-11823-2024>
- Taylor, T. E., Eldering, A., Merrelli, A., Kiel, M., Somkuti, P., Cheng, C., et al. (2020). OCO-3 early mission operations and initial (vEarly) XCO<sub>2</sub> and SIF retrievals. *Remote Sensing of Environment*, 251, 112032. <https://doi.org/10.1016/j.rse.2020.112032>
- Taylor, T. E., O'Dell, C. W., Baker, D., Bruegge, C., Chang, A., Chapsky, L., et al. (2023). Evaluating the consistency between OCO-2 and OCO-3 XCO<sub>2</sub> estimates derived from the NASA ACOS version 10 retrieval algorithm. *Atmospheric Measurement Techniques Discussions*, 2023(12), 1–61. <https://doi.org/10.5194/amt-16-3173-2023>
- Tu, Q., Hase, F., Schneider, M., García, O., Blumenstock, T., Borsdorff, T., et al. (2022). Quantification of CH<sub>4</sub> emissions from waste disposal sites near the city of Madrid using ground-and space-based observations of COCCON, TROPOMI and IASI. *Atmospheric Chemistry and Physics*, 22(1), 295–317. <https://doi.org/10.5194/acp-22-295-2022>
- van der Velde, I. R., van der Werf, G. R., Houweling, S., Maasakkers, J. D., Borsdorff, T., Landgraf, J., et al. (2021). Vast CO<sub>2</sub> release from Australian fires in 2019–2020 constrained by satellite. *Nature*, 597(7876), 366–369. <https://doi.org/10.1038/s41586-021-03712-y>
- Vogel, F. R., Frey, M., Staufer, J., Hase, F., Broquet, G., Xueref-Remy, I., et al. (2019). XCO<sub>2</sub> in an emission hot-spot region: The COCCON Paris campaign 2015. *Atmospheric Chemistry and Physics*, 19(5), 3271–3285. <https://doi.org/10.5194/acp-19-3271-2019>
- Wesloh, D., Lauvaux, T., & Davis, K. J. (2020). Development of a mesoscale inversion system for estimating continental-scale CO<sub>2</sub> fluxes. *Journal of Advances in Modeling Earth Systems*, 12(9), e2019MS001818. <https://doi.org/10.1029/2019MS001818>
- Wu, D., Lin, J. C., Fasoli, B., Oda, T., Ye, X., Lauvaux, T., et al. (2018). A Lagrangian approach towards extracting signals of urban CO<sub>2</sub> emissions from satellite observations of atmospheric column CO<sub>2</sub> (XCO<sub>2</sub>): X-Stochastic Time-Inverted Lagrangian Transport model (“X-STILT v1”). *Geoscientific Model Development*, 11(12), 4843–4871. <https://doi.org/10.5194/gmd-11-4843-2018>
- Wu, L., Bocquet, M., Lauvaux, T., Chevallier, F., Rayner, P., & Davis, K. (2011). Optimal representation of source-sink fluxes for mesoscale carbon dioxide inversion with synthetic data. *Journal of Geophysical Research*, 116(D21). <https://doi.org/10.1029/2011JD016198>
- Wunch, D., Toon, G. C., Blavier, J.-F. L., Washenfelder, R. A., Notholt, J., Connor, B. J., et al. (2011). The total carbon column observing network. *Philosophical Transactions of the Royal Society A: Mathematical, Physical & Engineering Sciences*, 369(1943), 2087–2112. <https://doi.org/10.1098/rsta.2010.0240>
- Xu, Y. (2023). *Analysis of atmospheric CO<sub>2</sub> measurements in Mexico City* (Theses). Université Paris-Saclay. Retrieved from <https://theses.hal.science/tel-04102800>
- Yadav, V., Ghosh, S., & Miller, C. E. (2023). Metrics for evaluating the quality in linear atmospheric inverse problems: A case study of a trace gas inversion. *Geoscientific Model Development*, 16(17), 5219–5236. <https://doi.org/10.5194/gmd-16-5219-2023>
- Yadav, V., & Michalak, A. (2013). Improving computational efficiency in large linear inverse problems: An example from carbon dioxide flux estimation. *Geoscientific Model Development*, 6(3), 583–590. <https://doi.org/10.5194/gmd-6-583-2013>
- Yang, E. G., Kort, E. A., Wu, D., Lin, J. C., Oda, T., Ye, X., & Lauvaux, T. (2020). Using space-based observations and Lagrangian modeling to evaluate urban carbon dioxide emissions in the middle east. *Journal of Geophysical Research: Atmospheres*, 125(7), e2019JD031922. <https://doi.org/10.1029/2019JD031922>
- Zhao, X., Chen, J., Marschall, J., Galkowski, M., Hachinger, S., Dietrich, F., et al. (2022). Understanding greenhouse gas (GHG) column concentrations in Munich using WRF. *Atmospheric Chemistry and Physics Discussions*, 1–30. <https://doi.org/10.5194/acp-2022-281>
- Zhao, X., Marshall, J., Hachinger, S., Gerbig, C., Frey, M., Hase, F., & Chen, J. (2019). Analysis of total column CO<sub>2</sub> and CH<sub>4</sub> measurements in Berlin with WRF-GHG. *Atmospheric Chemistry and Physics*, 19(17), 11279–11302. <https://doi.org/10.5194/acp-19-11279-2019>
- Zheng, T., Nassar, R., & Baxter, M. (2019). Estimating power plant CO<sub>2</sub> emission using OCO-2 XCO<sub>2</sub> and high resolution WRF-Chem simulations. *Environmental Research Letters*, 14(8), 085001. <https://doi.org/10.1088/1748-9326/ab25ae>
- Zhou, M., Ni, Q., Cai, Z., Langerock, B., Nan, W., Yang, Y., et al. (2022). CO<sub>2</sub> in Beijing and Xianghe observed by ground-based FTIR column measurements and validation to OCO-2/3 satellite observations. *Remote Sensing*, 14(15), 3769. <https://doi.org/10.3390/rs14153769>